NOVEL METHODS FOR SCATTER CORRECTION AND DUAL ENERGY IMAGING IN CONE-BEAM CT

A Dissertation
Presented to
The Academic Faculty

by

Xue Dong

In Partial Fulfillment
of the Requirements for the Degree
Doctor of Philosophy in the
School of Mechanical Engineering

Georgia Institute of Technology
May, 2014

NOVEL METHODS FOR SCATTER CORRECTION AND DUAL ENERGY IMAGING IN CONE-BEAM CT

Approved by:

Dr. Lei Zhu, Advisor
School of Mechanical Engineering
Georgia Institute of Technology

Dr. Ioannis Sechopoulos
Department of Radiology and Imaging Sciences
Emory University

Dr. C.-K. Chris Wang
School of Mechanical Engineering
Georgia Institute of Technology

Dr. Xiangyang Tang
Department of Radiology and Imaging Sciences
Emory University

Dr. Timothy H. Fox
Department of Radiation Oncology
Emory University

Date Approved: March, 2014

ACKNOWLEDGEMENTS

I would like to express my deepest gratitude to my advisor, Dr. Lei Zhu, who taught, guided, and encouraged me during the course of my graduate study. Without his encouragement, support and patience, this work would not have been possible.

I would also like to thank my Ph.D. reading committee, Dr. C.-K. Chris Wang, Dr. Timothy H. Fox, Dr. Ioannis Sechopoulos and Dr. Xiangyang Tang for their valuable participation and input in reviewing this dissertation.

I would like to give my appreciation to Dr. Tianye Niu for his encouragement and help during my Ph.D. study. I would like to thank my colleagues, Dr. Qiyong Fan and Mr. Michael Petrongolo for the useful discussions on various research topics. I would like to thank all the group members in Medical Imaging and Radiation Therapy Laboratory (MIRTL) for their support, patience and collaborations.

I am especially grateful to my beloved husband, Feng Wang for his emotional support, encourage and love throughout my Ph.D. studies. I wish to thank my parents and brother for their endless love, continued encouragement and support throughout my life, and all the sacrifices they made to help me pursue my dreams. In addition, I want to thank my entire extended family for their support and love.

TABLE OF CONTENTS

LIST OF TABLES

Page

LIST OF FIGURES

LIST OF SYMBOLS AND ABBREVIATIONS

α	projection angle of x-ray source
β	weight on image regularization
θ	angle of x-ray in transverse direction
φ	angle of x-ray in axial direction
μ	mean reconstructed value inside region of interest
$\bar{\mu}$	mean reconstructed value in reference image
a, b, c, d	elements of image-domain decomposition matrix
$d_{1/2}$	basis material image, or decomposed image
e	estimated electron density inside region of interest
$\bar{e}$	ground-truth value of electron density inside region of interest
$m_{H/L}$	measured projection at high/low tube energy
$n_{1/2}$	noise on decomposed image
$n_{pH/L}$	noise on raw projection at high/low tube energy
$n_{H/L}$	noise on CT image at high/low tube energy
S	beam blocker sampling period
W	beam blocker strip width
$x_{H/L}$	reconstructed CT image at high/low tube energy

ABOCS	accelerated barrier optimization for compressed sensing
CBCT	cone-beam CT
CNR	contrast-to-noise ratio
CS	compressed sensing
DECT	dual-energy CT

DQE	detection quantum efficiency
FBP	filtered back-projection
FOV	field of view
GPU	graphics processing unit
GP-BB	gradient projection with an adaptive Barzilai–Borwein selection scheme
HU	hounsfield unit
IGRT	image-guided radiation therapy
kV	kilovoltage
MC	Monte Carlo
MDCT	multi-detector CT
MTF	modulation transfer function
OBI	on-board imager
PWLS	penalized weighted least-squares
q-GGMRF	*q*-generalized Gaussian Markov random field
RMSE	square root of mean square error
ROI	region of interest
SNR	signal-to-noise ratio
SNU	spatial nonuniformity
SPR	scatter-to-primary ratio
TV	total variation

SUMMARY

Excessive imaging doses from repeated scans and poor image quality mainly due to scatter contamination are the two bottlenecks of cone-beam CT (CBCT) imaging. This study investigates a method that combines measurement-based scatter correction and a compressed sensing (CS)-based iterative reconstruction algorithm to generate scatter-free images from low-dose data. Scatter distribution is estimated by interpolating/extrapolating measured scatter samples inside blocked areas. CS-based iterative reconstruction is finally carried out on the under-sampled data to obtain scatter-free and low-dose CBCT images. In the tabletop phantom studies, with only 25% dose of a conventional CBCT scan, our method reduces the overall CT number error from over 220 HU to less than 25 HU, and increases the image contrast by a factor of 2.1 in the selected ROIs.

Dual-energy CT (DECT) is another important application of CBCT. DECT shows promise in differentiating materials that are indistinguishable in single-energy CT and facilitates accurate diagnosis. A general problem of DECT is that decomposition is sensitive to noise in the two sets of projection data, resulting in severely degraded qualities of decomposed images. The first study of DECT is focused on the linear decomposition method. In this study, a combined method of iterative reconstruction and decomposition is proposed. The noise on the two initial CT images from separate scans becomes well correlated, which avoids noise accumulation during the decomposition process. To fully explore the benefits of DECT on beam-hardening correction and to reduce the computation cost, the second study is focused on an iterative decomposition method with a non-linear decomposition model for noise suppression in DECT. Phantom results show that our methods achieve superior performance on DECT imaging, with respect to noise reduction and spatial resolution.

CHAPTER 1

INTRODUCTION

1.1 Cone-beam CT imaging

X-ray kilovoltage (kV) cone-beam CT (CBCT) imaging is being increasingly used in various clinical applications, mainly for its large volume coverage and hardware compatibility with open-gantry x-ray imaging system [1-5]. For example, on-board CBCT on a radiation therapy machine enables dose verification, patient positioning and tumor targeting in image-guided radiation therapy (IGRT) [6-8]. C-arm CBCT provides image guidance which is critical in surgical procedures [9, 10]. There is also an explosion of interest in CBCT in clinical dental practice, where CBCT allows the creation of real-time imaging in axial, coronal and sagittal planes, and provides 3D radiographic information [11, 12].

Figure 1.1 shows the on-board imager system developed by Varian Medical System (Palo Alto, CA). The CBCT system is combined with the linear accelerator, and is used to locate tumors and calculate radiation dose. Figure 1.2 shows anther CBCT system, the Siemens Artis Zeego C-arm system. The C-arm system provides near-real-time 3D imaging and real-time fluoroscopy, which is used in operation rooms to provide image guidance in surgical procedures.

1.2 Limitations of cone-beam CT

Despite the rapid expansion of clinical applications, the current CBCT technology has limitations. Scatter contamination, excessive image dose and beam-hardening artifacts are three major limitations that hinder the wide application of CBCT.

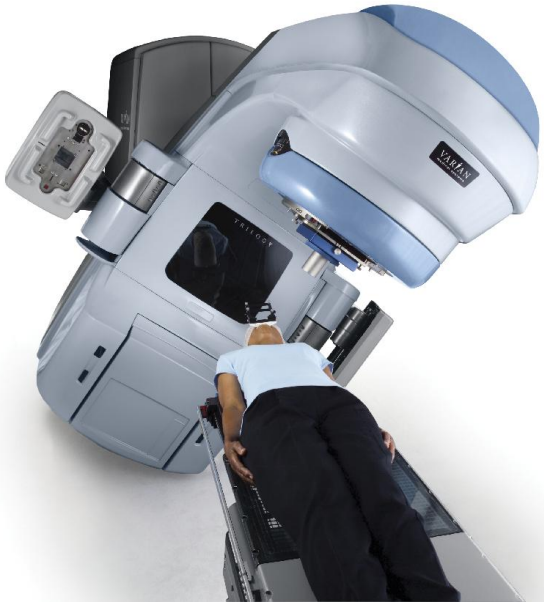

Figure 1.1 The on-board imager device mounted on Trilogy® medical linear accelerator. (http://newsroom.varian.com/Trilogy?mode=gallery)

Figure 1.2 The Siemens Artis Zeego C-arm CBCT system. (http://www.siemens.com/press/en/pressrelease/?press=/en/pressrelease/2008/imaging_it/medax200801025.htm)

1.2.1 Scatter contamination

Scatter artifact is considered as one of the fundamental limitations of CBCT [5]. CBCT imaging on a human body could result in scatter-to-primary (SPR) typically over 2 [13]. High intensity of scatter signals causes severe cupping and streak artifacts, reduced accuracy in reconstruction values, as well as degradation of contrast-to-noise ratio (CNR), which hampers the application of CBCT [14-16]. Figure 1.3 shows the comparison of CBCT and diagnostic CT images of the same patient. This diagnostic CT system has an estimated maximum SPR of ~0.01 on patients due to the small axial coverage [17], and the images are used as scatter-free references. As the white arrows indicate, large shading errors are seen in the CBCT images (Figure 1.3 (a)). Some fine structures present in the diagnostic CT images are also buried in the artifacts (Figure 1.3 (c)) due to the CNR loss.

Generally, the number of scattering events is proportional to the illumination volume size. For example, Siewerdsen *et al.* performed phantom studies with flat-panel cone-beam CT, and found that large cone angles result in significant shading artifacts as well as increased CT number errors [18]. Endo *et al.* observed similar results on a 256-slice multidetector CT scanner. The estimated SPR was drastically decreased with small cone angle, and increased nearly twice as the diameter of a cylindrical phantom increases from 200 mm to 350 mm [17]. Global cupping artifacts and local streaking artifacts are the two major types of artifacts caused by scatter contamination. The global cupping artifacts result from the facts that scattered radiation increases the overall signal intensity of the projections, thus, the reconstructed object is less attenuating than the real one. The local streaking artifacts are majorly observed in the areas where the object is highly attenuated and the intensity of the corresponding primary signal is small. Simulation studies showed that the CT number errors are more than 350 hounsfield unit (HU), and streaking artifacts are up to 100 HU with an SPR of 2 [5].

Increased SPR not only causes the decrease of CT number accuracy, but also the degradation of CNR. Wang *et al.* found a relationship between CNR with and without

scatter correction for a small SPR, which shows that increased SPR results in a decrease of CNR [19]. Note that, loss of CNR can be compensated with increased imaging dose. However, additional imaging dose is not practical in clinical applications, since CNR is approximately proportional to the square root of x-ray imaging dose [20].

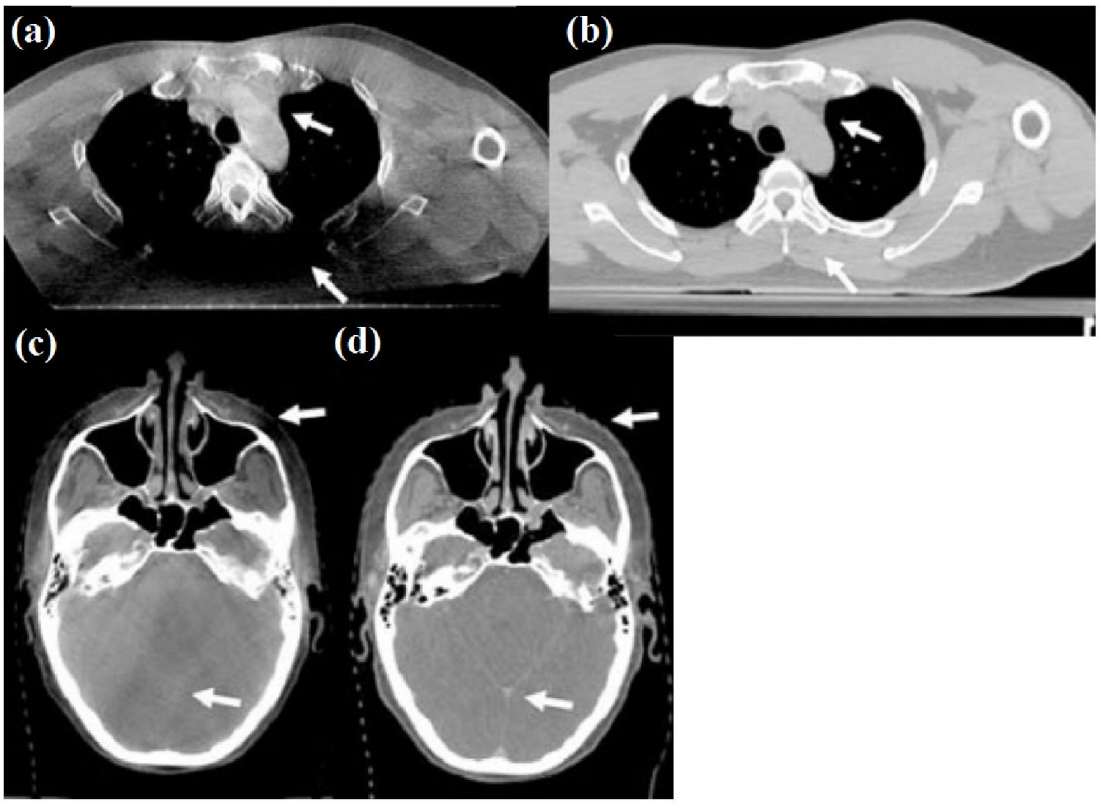

Figure 1.3 CBCT and diagnostic CT of the same patient. (a) CBCT of chest; (b) diagnostic CT of chest; (c) CBCT of head; (d) diagnostic CT of head. Display window: (a)&(b): [-500 500] HU; (c)&(d) [-335 655] HU. The white arrows highlight the differences of the images.

Based on whether scatter signals are directly measured or not, the existing scatter correction methods can be divided into two major categories: measurement-based methods and non-measurement-based methods. Measurement-based methods measure the scatter signals with an insertion of a beam blocker [21-24]. These methods are easy to implement, and obtain accurate scatter estimation. However, the beam blocker attenuates

primary projections, thus an accurate reconstruction is impossible with conventional reconstruction method if the blocked primary is not compensated for. Non-measurement-based methods estimate scatter signals with the knowledge of the system geometry and imaged object [25-29], or prevent scattered radiation from reaching the detector, typically by using an anti-scatter grid or increasing air gap between patient and detector [30-36]. These methods have shown success on scatter correction and suppression, but the application is limited in clinical practice. Deterministic scatter models typically approximate the scatter distribution as a convolution of primary signals with a scatter kernel. This method achieves a satisfactory accuracy of scatter estimation, but the efficacy is generally limited. Monte Carlo (MC) simulation obtains more precise scatter estimation. However, the intense computation makes it unpractical in clinical applications. Air gap requires no special algorithms or additional hardware, but increasing the distance between patient and detector is infeasible in many clinical applications. Furthermore, due to the increase of object-to-detector distance, extra imaging dose is required to maintain the same level of x-ray flux on the detector. Anti-scatter grid shows limited efficiency on scatter correction. Meanwhile, the insertion of anti-scatter grid results in inevitable primary loss, which requires increased x-ray dose to compensate for.

1.2.2 Imaging dose

CT imaging dose becomes an increasing public concern nowadays. The risk of radiation-induced cancer is important, especially when sizeable patient data are acquired and/or when repeated scans are performed on the same patient. Dose control is more demanding on volumetric CT systems, which are susceptible to scatter contamination due to the large illumination field. As a fundamental limitation, scatter reduces image contrasts and therefore large dose is required for a clinically useful contrast-to-noise ratio. These challenges are seen in on-board CBCT on a radiation therapy machine, which is used for precise tumor targeting at treatment time. Although CBCT improves the

performance of image guided radiation therapy, the benefits of its daily use during a treatment course of 4-6 weeks are counteracted by excessive x-ray imaging doses. The repeated CBCT scans during a fractionated treatment course produce high dose to healthy organs, which is up to 5~10 cGy per scan and 100~300 cGy per treatment course [37-42].

Recent development on the CT data acquisition can significantly lower the imaging dose without degrading image quality. For example, automatic exposure control adaptively adjusts the tube current depending on the magnitude of the detected projection such that the noise variance is more uniform on the CT images [43-46]. Detectors with better detection quantum efficiencies (DQE) obtain images with higher signal-to-noise ratios (SNR) for the same imaging dose [47, 48]. The advances in data processing and reconstruction algorithms provide an alternative approach on substantial dose reduction. Noise suppression methods are able to maintain the SNR level with reduced tube current or pulse duration (i.e. mAs) [49-52]. Advanced CT reconstruction algorithms present advantages on further reducing the imaging dose by decreasing the data acquisition. By modeling the physical process of a CT scan, including scattering, beam-hardening, and statistical fluctuation, iterative reconstruction algorithms are more resistant to noise and therefore require less dose [49, 53-55]. With prior patient knowledge, which cannot be easily incorporated in analytical reconstruction, iterative reconstruction obtains high-quality images even on insufficient data.

1.2.3 Beam-hardening artifacts

Beam-hardening artifacts arise from the inherent poly-energetic nature of the x-ray beam generated by current commercial x-ray tubes on an onboard CBCT system. The mean energy of the x-ray beam increases as it penetrates the object, since lower energy photons are absorbed in preference to higher energy photons. The energy dependence of the object linear attenuation coefficients makes line integral measurements inaccurate, leading to shading artifacts and streak artifacts appeared between two dense objects (e.g.

bones), with CT number errors of up to 100 HU [56, 57]. To better view the scatter and beam-hardening artifacts separately, we carried out a head phantom study on a tabletop CBCT system with a 120 kVp source. Besides the CBCT scan (Figure 1.4 (a)), a second scan was performed with a narrowly open collimator – a fan-beam equivalent geometry – to suppress the scatter signal (Figure 1.4 (b)). The fan-beam CT image is considered to contain beam-hardening artifacts only. To obtain a reference image without beam-hardening effects, we used the same fan-beam geometry and a 39 mm Al layer to heavily filter the x-ray beam in a third scan (Figure 1.4 (c)). The incident x-rays were close to mono-energetic, but significantly attenuated. The scan was therefore repeated twenty times and averaged to make the image noise matchable to that in Figure 1.4 (a) and (b). The comparison indicates that the beam-hardening artifacts (around 70 HU) are severe around high-intensity areas.

One way to alleviate the beam-hardening problem is to pre-filter the x-ray beam, which narrows the x-ray output spectrum. The performance of this physics-based approach is limited since a strong beam filter heavily attenuates the x-ray beam and therefore lowers the effective tube output. Furthermore, the mean energy of the x-ray spectrum increases after filtration, leading to reduction of image contrast and therefore low-contrast detectability. Many software-based methods have been proposed to combat beam-hardening effects on commercial CBCT systems. Beam-hardening errors include global cupping artifacts from the background low-intensity materials (e.g. tissue and water) and local shading artifacts from the high-intensity materials (e.g. bones). The global cupping from the background material can be effectively removed by assuming a single material for the whole object and applying correction on the projection data with a polynomial fitting or a lookup table [58]. This method performs well in most cases, but fails to remove the shading artifacts from the high-intensity objects. Iterative algorithms are able to achieve an improved beam-hardening correction when two or more materials are present in the object [56]. Nevertheless, the performance of these algorithms depends

on either accurate knowledge of the physical properties of the x-ray spectrum and detector response, or proper settings of empirical algorithm parameters. Dual energy imaging provides another solution to the beam-hardening problem [59-61]. Two basis materials images are decomposed from the data with two different x-ray spectra (e.g. with low and high tube kVp energies), and then are synthesized for a given single energy, which is free of beam-hardening artifacts.

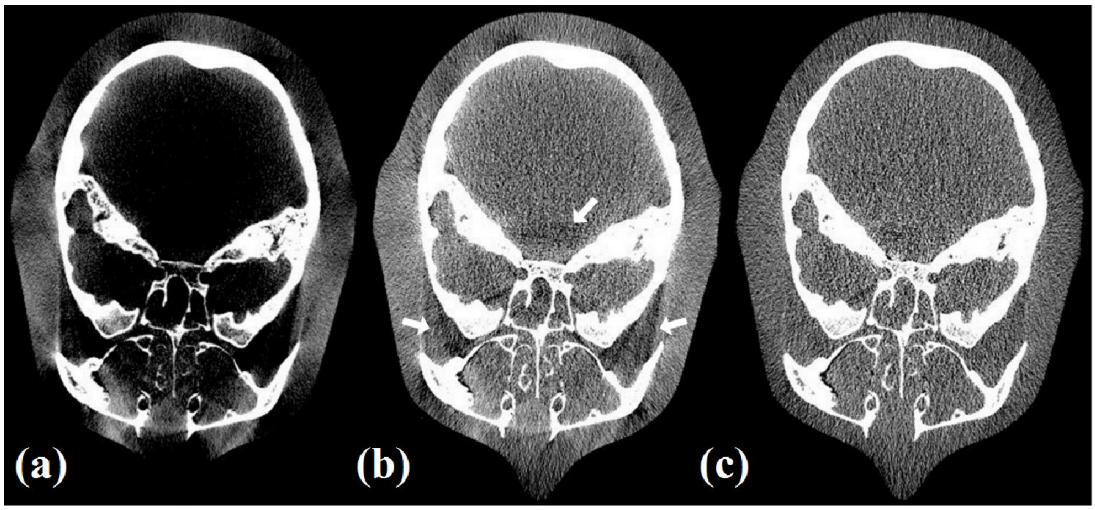

Figure 1.4 CT images of a head phantom on a flat-panel-based system. a) CBCT; b) fan-beam CT (with a narrowly open collimator to suppress scatter); c) fan-beam CT with a 39 mm Al beam filter to suppress beam-hardening effects. Display window: [-100 200] HU.

1.3 Dual energy CT

Since the development of dual energy CT (DECT) in 1976, DECT has attracted increasing attention due to its capability of providing material decomposition, energy selective imaging as well as correcting for beam-hardening artifacts [59, 62-64]. DECT has the potential to distinguish material which cannot be separated with conventional single energy CT. DECT provides important diagnostic information in various clinical applications. For example, in the head and neck area, dual energy methods remove bone from CT angiography and resolve the superimposition of bone and vessels [65]. In the assessment of lung perfusion, dual energy method obtains an equivalent clinical

information, but significantly reduced imaging dose compared to dynamic CT [66]. In the abdomen area, the material decomposition of DECT is capable of identifying renal stones based on their composition, and of improving the lesion detections [67].

Dual energy imaging is based on the characteristic of attenuation coefficient over the diagnostic energy range where Rayleigh scattering can be ignored. In this energy range, the linear attenuation coefficient of any material is a weighted summation of two universal energy dependent basis functions accounting for photoelectric and Compton interactions. In practical implementations, the basis functions of the decomposition can be the energy-dependent linear attenuation coefficients of two different actual or even virtual materials (e.g. tissue and bone). This signal decomposition can be implemented on either raw projections or reconstructed images. With projection-domain decomposition, the weights of the two basis functions are uniquely determined from measured projections with two different x-ray spectra. Their spatial distributions are then reconstructed using the same CT principle. As the calculated weights are energy-independent, these two images are free of beam-hardening artifacts. Image-domain decomposition implements a linear transformation on the CT images reconstructed from dual energy projections, which also provides material decomposition information. Compared to projection-domain method, which often requires the knowledge of x-ray spectra and detector response, or employs a relatively complex non-linear decomposition model, image-domain method is easier to implement, thus more commonly used in clinical applications. On the other hand, projection-domain decomposition obtains images with better quality, since it effectively removes beam-hardening errors [59-61].

DECT requires scans with two different x-ray tube energies, i.e. one with high energy and one with low energy. A straightforward method for dual energy data acquisition is to obtain two sets of CT data from two rotations with two different x-ray spectra [68]. This method requires no additional hardware, thus is of relatively low cost.

However, the method is of poor temporal resolution and is susceptible to motion artifacts. The recent advances of new CT imaging systems revolutionize the way of the projection data acquisition. For example, dual-source CT systems are able to simultaneously acquire two orthogonal projections with different x-ray energies [69, 70]. The fast kVp switching CT rapidly switches the x-ray tube voltage between two settings (e.g. 80 kVp and 140 kVp) during the data acquisition in one scan [71]. Implementations of dual-energy methods become practical on these systems. The development of energy-resolving detectors also makes energy-selective reconstruction possible on projection data from one single scan [72, 73].

1.4 Main contributions and publications

Most of the work can be found in the following journal papers and conference proceedings:

- **Xue Dong**, Tianye Niu, Lei Zhu, *"Relationship between x-ray illumination volume size and flat field intensity and its impacts on x-ray imaging"*, Medical Physics, 39(10):5901-5909, 2012.
- **Xue Dong**, Michael Petrongolo, Tianye Niu, Lei Zhu, *"Low-dose and scatter-free cone-beam CT imaging using a stationary beam blocker in a single scan: phantom studies",* Computational and Mathematical Methods in Medicine, Volume 2013 (2013), 637614.
- Tianye Niu, **Xue Dong**, Michael Petrongolo, Lei Zhu, *"Iterative image-domain decomposition for dual-energy CT"*, Medical Physics, 41(4):041901, 2014.
- **Xue Dong**, Tianye Niu, Lei Zhu, *"Combined iterative reconstruction and image-domain decomposition for dual energy CT using total-variation regularization"*, Medical Physics (in press).
- **Xue Dong,** Xun Jia, Tianye Niu, Lei Zhu, "*Low-dose and scatter-free cone-beam CT imaging: a preliminary study*", Proc. SPIE 8313, 831319 (2012)
- **Xue Dong,** Tianye Niu, Lei Zhu, "Single-scan energy-selective imaging on cone-beam CT: a preliminary study", Proc. SPIE 8668, 86682Z (2013)

as well as conference presentations:

- **Xue Dong,** Tianye Niu, Lei Zhu, "*Relationship between x-ray illumination volume size and flat field intensity and its impacts on x-ray imaging*", 2011 Joint AAPM & COMP conference, Vancouver, Canada.
- **Xue Dong,** Tianye Niu, Lei Zhu, "*Single-scan energy-selective imaging on cone-beam CT: a phantom study*", 2013 Varian Research Partnership Symposium , Atlanta, GA.
- **Xue Dong,** Tianye Niu, Lei Zhu, "*Iterative reconstruction for dual energy CT using accelerated barrier optimization compressed sensing (ABOCS)* ", 2013 AAPM, Indianapolis, IN.

At the time of this writing, the results in Chapter 4 have not been published, and a journal paper submission is in preparation.

1.5 Outline of this dissertation

The dissertation is organized in the following manner:

Chapter 1 presents the background and scope of this dissertation, and outlines the dissertation.

Chapter 2 discusses the scatter correction and dose reduction methods in CBCT. A novel method that combines measurement-based scatter correction and CS-based iterative reconstruction is proposed to generate scatter-free images from low-dose projections.

Chapter 3 investigates the noise boost problem in DECT, and presents a new method for noise suppression in DECT with image-domain decomposition.

Chapter 4 explores the benefits of DECT on beam-hardening correction, and expands the framework of an iterative de-noising method to include a non-linear decomposition model for noise suppression in DECT.

Chapter 5 summarizes the dissertation and suggests directions for future research.

Finally, Appendix explains the deviation of noise-covariance matrix of the observation with a non-linear decomposition model.

CHAPTER 2

LOW-DOSE AND SCATTER-FREE CONE-BEAM CT IMAGING USING A STATIONARY BEAM BLOCKER IN A SINGLE SCAN

2.1 Introduction

On-board cone-beam CT (CBCT) is being increasingly implemented on radiation therapy machines for accurate patient positioning and tumor targeting in image-guided radiation therapy (IGRT). The use of CBCT increases patient setup accuracy, and also opens possibilities of CBCT-based accurate tumor delineation and therapeutic dose calculation. Nevertheless, the wide application of CBCT in IGRT is limited by excessive imaging dose and poor image quality.

The repeated CBCT scans during the treatment procedure produce high dose to healthy organs. It has been reported that the dose delivered from a CBCT system could be as high as 5~10 cGy per scan and 100~300 cGy per treatment course [37-42]. Although radiotherapy patients are being exposed to higher radiation doses for cancer treatment, the additional CBCT dose leads to skin burns, cataracts and increased risks of radiation-induced cancer or genetic defects [37]. Moreover, the CBCT dose is particularly risky for radiation-sensitive groups [41]. For example, CBCT-guided radiation therapy is essentially prohibitive for pediatric patients, resulting in suboptimal treatment outcomes. Patient dose can be lowered by optimizing both hardware and software designs of the CT systems. Existing approaches include optimization of data acquisition protocols (e.g automatic exposure control), improvement of detector quantum efficiency, region-of-interest (ROI) reconstruction [74] from reduced projections, and noise suppression with degraded spatial resolution. However, after continuous development of CT systems for

decades, further dose reduction from these techniques is limited or costly. Decreasing the total number of incident photons of each projection ray (i.e. mAs) and reducing the number of x-ray projections also lower the patient dose, but with degraded image quality in the conventional filtered back-projection (FBP) reconstruction [75]. Recent advances in compressed sensing (CS) enable accurate CT image recovery from under-sampled data [76]. Compared to analytical algorithms, total variation (TV)-based CS methods [53, 77] have demonstrated significant improvements in both fan-beam and cone-beam CT reconstruction especially when projection data are under-sampled with sparse views [54, 77, 78] or with missing data in a single view [77]. These reconstruction algorithms minimize the TV of CT image constrained by data fidelity and image non-negativity, which show promise in reducing CT dose without significantly degrading image qualities.

Besides excessive patient dose, CBCT images are also subject to severe contamination from scatter radiation. Scatter signals induce large image artifacts and CT number nonlinearity, which limit the applications of CBCT. For a middle-size human torso, the average scatter-to-primary ratio (SPR) is around 2~3, which leads to CT number errors up to 350 HU [13, 79-81]. Extensive studies have been conducted on scatter correction techniques. These published techniques can be divided into two major categories, based on whether scatter signals are directly measured or not. Non-measurement-based methods either prevent scattered radiation from reaching the detector (for example, using an anti-scatter grid [32, 82], limiting the field of view (FOV), and increasing the air gap between the object and the detector [83]) or predict the scatter distribution (using, for example, analytical modeling [84], modulation methods [85-88], and Monte Carlo (MC) simulation [89, 90]). These methods improve the image quality to a certain extent, but their performances are limited in clinical applications [5]. An anti-scatter grid results in primary signal loss, thus increases image noise and degrades image qualities [32, 82]. The air-gap between the object and the detector is limited by the size of operation room [83]. Monte Carlo simulation generates accurate scatter signals but is

computationally intensive [89, 90]. On the other hand, methods of direct scatter measurement conveniently obtain accurate scatter estimates with negligible computational cost [81]. In the measurement-based method, a beam blocker is typically inserted between the x-ray source and the object, and scatter signals are estimated inside the detector shadows of the beam blocker [22, 79, 91, 92], where primary signals are fully attenuated. The scatter distribution of the whole field is then obtained via interpolation/extrapolation on the scatter samples inside the shadows, since scatter distributions have dominant low-frequency components [79, 93, 94]. The method achieves accurate scatter estimation without prior knowledge of x-ray source, object, imaging geometry, and is easy to implement. Nonetheless, primary signal loss is inevitable due to the insertion of the beam blocker. As a result, severe image artifacts appear in the conventional reconstruction [95] if the missing primary signals are not compensated for [81]. Two projections per view, one with the blocker and the other without [13], or moving blockers during the scan [96], are designed to compensate for the primary loss. These hardware modifications complicate the data acquisition, and increase scan time and patient dose. Recently, our group developed a "crossing-finger"-shape beam blocker, which makes use of the data redundancy condition in a 360° full-fan CT scan. This method achieves accurate scatter estimation and reconstruction within one single scan, and thus is considered clinically more attractive. Though demonstrated promising, the "crossing-finger"-shape blocker is of complex structure, and the insertion of beam blocker complicates the FBP reconstruction algorithm.

For years research has been developed independently on dose reduction and scatter correction. Nevertheless, little effort has been devoted to exploit the full potential of image improvement from a combination of the above two schemes. Scatter measurement accurately corrects for scatter but leads to primary loss, which makes most of the measurement-based correction methods unpractical. CS-based iterative algorithm lowers imaging doses and obtains accurate reconstruction even on the insufficient data from

sparse views or a reduced number of detector pixels. Considering the complimentary capabilities of these two approaches, we use an improved stationary beam blocker in the CBCT system for simultaneous dose reduction and scatter measurement, and an iterative algorithm for accurate reconstruction on the projections with missing data in a single scan. The new method explores the strengths of measurement-based scatter correction and iterative reconstruction while eliminating their shortcomings, and obtains low-dose and scatter-free CBCT images.

In the new method, the lead strips of the blocker are placed in the longitudinal direction and located asymmetrically with respect to the central longitudinal line of the detector. If one ray is blocked by the strip, its conjugate is still measured after around 180° rotation even if it is in the off-plane. The beam blocker is inserted between the x-ray source and the object, where scatter distribution is obtained by interpolation/extrapolation on the scatter samples inside the strip shadow. The insertion of blocker also reduces patient dose since x-ray primary signals are attenuated [97]. The patient dose is further reduced by decreasing the number of projections. Our recently developed CS-based iterative reconstruction, accelerated barrier optimization for compressed sensing [75], is carried out on the blocked data to obtain scatter-free and low-dose CBCT images. Simulation studies are designed on the Shepp-Logan phantom to optimize the lead strip geometry and the required number of projections for a certain dose reduction ratio, by comparing the CT image accuracy. The performance of the method is evaluated on the Catphan©600 phantom and an anthropomorphic head phantom.

2.2. Method

2.2.1 Blocker design

In a circular CBCT scan, one projection ray can be specified by (θ,φ,α), where θ and φ are the angles of the ray in the transverse and axial directions respectively, and α is

the projection angle of the source. It can be easily verified that no projection rays are redundant in such geometry except those in the mid-plane (i.e. φ=0). Nevertheless, if a commonly-used approximation of small cone angle (i.e. $\varphi \approx 0$ for the whole projection) is used, the redundant rays have the following relationships:

$$\theta_1 = -\theta_2 \qquad \text{Equation 2.1}$$

$$|\alpha_1 - \alpha_2| + 2|\theta_1| = \pi \qquad \text{Equation 2.2}$$

With a full rotation and full object coverage, half of the CBCT projection data are considered to be redundant. Under the small-cone-angle approximation, each projection ray in a CBCT full scan has a corresponding redundant ray measured from the opposing direction. The two lines are referred to as a conjugate ray pair and this condition is referred to as data redundancy. Therefore, some of these redundant rays can be blocked for other purposes (e.g., scatter measurement) while still maintaining an accurate reconstruction [98]. No hardware compensation for the missing primary data is necessary and the data acquisition is complete with one single scan.

Guided by this principle, lead strips are placed in the longitudinal direction, which is perpendicular to the rotation plane, to block only redundant rays for scatter measurement. One ray blocked by the strip is measured through its conjugate after around 180° rotation. The beam blocker is designed to block less than 50% of full illuminated field and are placed asymmetrically with respect to the central longitudinal line of the detector, such that at least one ray from its conjugate ray pair can be measured on the detector. Note that, the central longitudinal line of the detector is always left unblocked to avoid the missing rays passing through the object center.

Figure 2.1 shows the geometry of the proposed method and our experimental setup. The designed blocker is placed between the x-ray source and the object. The lead strips are placed along the longitudinal direction and uniformly distributed in the lateral

direction. The strips have a thickness of around 3 mm and attenuate more than 99.99% of incident x-ray photons. Only scatter samples are measured inside the shadows on the detector. Besides the strip placement, two more parameters are needed in the blocker design: sampling period (S) and strip width (W). The strip width cannot be too small since the penumbra effects on the strips limit scatter measurement accuracy [99]. Moreover, wider blocker contributes more to the dose reduction. In this study, we choose a conservative W value of about 44 pixels (~ 17 mm) on detector. S is optimized by comparing the CT image quality for a certain dose reduction ratio.

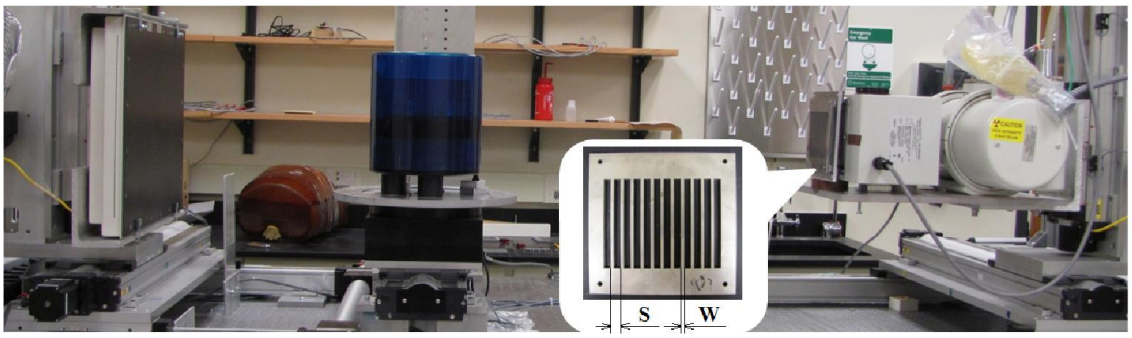

Figure 2.1 The CBCT tabletop system and Catphan©600 phantom. The designed blocker is mounted in front of the collimator and shown in an enlarged inset. The lead blocker is sandwiched between two layers of thin steel, each with a thickness of 0.2 mm, to improve the mechanical strength.

2.2.2 Scatter estimation and correction

As shown in our previous studies [80, 81, 87] and the literature [100], the insertion of the beam blocker does not greatly perturb the spatial frequency spectrum of scatter in cone-beam projections and scatter is still predominantly low-frequency. The whole field scatter distribution is therefore accurately estimated using interpolation/extrapolation on the measured samples. To avoid the penumbra effect of the strips, only the measured data inside the central two-third of the strip shadows are used in the scatter estimation. Since the lead strips cover the whole blocker in the longitudinal direction, a 1D cubic

interpolation is carried out on each lateral line to estimate the scatter distribution over the whole detector area. The estimated scatter is then subtracted from the raw projection to generate the scatter-corrected CBCT projections.

2.2.3 Reconstruction on incomplete data

These corrected CBCT projections are incomplete due to the insertion of the blocker and the angular under-sampling. Severe artifacts therefore appear in the conventional FBP reconstruction. To improve the image quality, the missing primary signals in the blocked area are compensated for using their conjugate rays. As described by Equation 2.1 and 2.2, the two detector points corresponding to the conjugate ray pair are symmetric with respect to the detector central longitudinal line, and their projection angle has a difference of π-2$|\theta|$. Due to the discretization of the data acquisition in both spatial and angular directions, the missing primary is compensated for using its conjugate point by interpolating on the scatter-corrected sinogram.

An in-house CS-based iterative reconstruction is applied to further improve the image quality. The algorithm is referred to as the accelerated barrier optimization for compressed sensing (ABOCS) reconstruction algorithm, which minimizes the image TV term with data fidelity and non-negativity constraints [75]. ABOCS formulates the TV minimization constrained by the data fidelity into a form similar to that of the conventional TV regularization but with an automatically adjusted penalty weight. The automatic penalty weight is controlled by the data fidelity tolerance, which is estimated from the raw projections according to the Poisson statistics, and the data error in the current iteration. Consistent reconstruction performances are achieved using the same algorithm parameters on scans with different noise levels and/or on different objects. The problem is then solved efficiently by gradient projection with an adaptive Barzilai–Borwein step-size selection scheme. Readers are referred to Ref. [75] for more details.

Note that, image noise increases significantly after scatter correction [13]. An additional penalized weighted least-squares (PWLS) algorithm [13] is performed to reduce the noise in the reconstructed images.

2.2.4 Evaluation

A small strip sampling period (S) increases the scatter estimation accuracy, but reduces the available data in a CT scan which may decrease the reconstruction accuracy. To balance the tradeoff, we first carry out simulation studies on the Shepp-Logan phantom to optimize S (therefore the projection number) for 80% dose reduction, by comparing the CT reconstruction accuracy with scatter correction. The image error is quantified as the percentage of root of mean square error (RMSE). The scatter is simulated using the Monte Carlo code (GEANT4 package) [101]. To save computation time, we use a uniform water ellipsoid with the same geometry as that of the Shepp-Logan phantom to generate the scatter distribution.

With the optimized S, we then evaluate the performance of the proposed method on the Catphan©600 phantom with a diameter of 200 mm (The Phantom Laboratory, Salem, NY) and an anthropomorphic head phantom on our CBCT table-top system. The geometry of this system exactly matches that of a Varian On-Board Imager (OBI) CBCT system on the TrueBeam radiation therapy machine. A detailed system configuration is described in Ref. [80]. The lead sheet of the designed blocker is first shaped using a waterjet cutting system. To improve the mechanical strength of the blocker, the lead is then sandwiched between two layers of thin steel (~ 0.2 mm) using J-B WELD epoxy adhesive (www.grainger.com).

CBCT images are compared with and without the proposed method. A total of 655 projections are acquired for the conventional FBP reconstruction. Few-view projection data are generated from the 655 projections with an evenly distributed angular spacing.

The estimated dose reduction ratio is calculated based on the number of measured projection lines [80]. The proposed method is compared with low-dose CBCT without scatter correction. Note that, the scatter estimation is also performed on the sparse projections.

For a quantitative error analysis, an additional set of projections is acquired with a fan-beam geometry, which narrows the collimator open width to around 10 mm on the detector for inherent scatter suppression. The resultant images are used as references. Image quality metrics are used to quantitatively evaluate the performance of the proposed method. For the selected region of interest (ROI), the CT number error is calculated as the square root of the mean square error (RMSE) and defined as

$$\mathrm{RMSE} = \sqrt{\frac{1}{N_{ROI}} \sum_{i=1}^{N_{ROI}} (\mu_i - \overline{\mu_i})^2} \qquad \text{Equation 2.3}$$

where i represents the index of ROI and μ_i is the mean reconstructed value inside the ROIs, and $\overline{\mu_i}$ is the value in the reference image, and N_{ROI} is the total number of ROIs. The image contrast is calculated as

$$contrast = |\mu_r - \mu_b| \qquad \text{Equation 2.4}$$

where μ_r is the mean reconstructed value inside the ROI and μ_b is the mean reconstructed value in the surrounding area.

2.3 Results

2.3.1 Optimization of blocker sampling period

Figure 2.2 shows RMSE of scatter estimation and reconstructed image with respect to different sampling period (S) on the detector. The imaging dose reduction is 80%, and the CT number error reaches the minimum when S is about 50 mm. Larger sampling period degrades the image quality due to the increased scatter estimation error. Smaller sampling period also deteriorates the image because of relatively more primary signal

loss in each projection. In the following studies, we choose a sampling period as about 52 mm on the detector, and the W is chosen as about 17 mm on the detector, which blocks 33% of the illuminated area. In both phantom studies, we use one third of total 655 projections, which is 219 projections. By blocking 33% of illuminated area in each of 219 projection, the proposed method achieves the dose reduction ratio of around 75%. 163 projections are used in low-dose CBCT without scatter correction to obtain the same dose reduction.

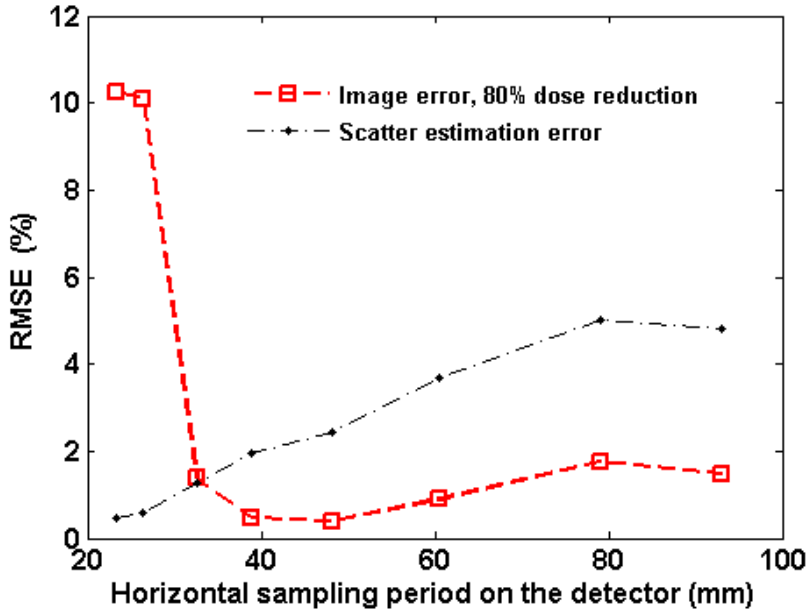

Figure 2.2 The reconstructed image and scatter estimation error for different sampling periods calculated on the projection of the Shepp-Logan phantom.

2.3.2 Catphan©600 phantom results

Figure 2.3 shows the 1D horizontal profiles of scatter signals, raw projections and line integrals of one projection on the Catphan©600 phantom. The reference scatter signals are obtained as the difference of the cone-beam and fan-beam projections. As seen in Figure 2.3 (a), the estimated scatter profile using our method matches well with the reference in the central region pixels (250-800) with an estimation error of less than

6.5%. Relatively large deviations are found around and outside the phantom boundary. However, the intensity of primary signals in these areas is high, which leads to a negligible estimation error of line integral. Figure 2.3 (b) shows the line integrals with and without the proposed method. The blue circles indicate the scatter corrected primary signals measured in the illuminated area. The missing primary signals due to the insertion of the beam blocker are compensated with their conjugate rays analytically and shown as the green triangles in Figure 2.3(b). Our method significantly enhances the intensities of the line integrals, which are close to those of the ground-truth, i.e., fan-beam CT.

Figure 2.4 shows the reconstructed image with and without the proposed low-dose and scatter-free CBCT imaging scheme. Figure 2.5 shows the comparison of 1D profiles passing through two high contrast rods inside the phantom, as indicated by the red line in Figure 2.4(d). Without scatter correction, the ABOCS reconstruction reduces the dose by 75%, however, severe shading artifacts are still observed (see Figure 2.4(b) and Figure 2.5). Our proposed method significantly suppresses the shading artifacts (see Figure 2.4(c)). After improvement, the image quality is comparable to that of the reference (i.e., fan-beam CT in Figure 2.4(d)). For the quantitative evaluation of the performance using our method, the average CT numbers and contrasts are calculated for the contrast rods in one of the phantom slice. The results are summarized in Table 2.1 using those from the fan-beam CT as the references. In the selected ROIs, the proposed method reduces the mean CT number error from over 250 HU to around 24 HU, and increases the contrast by a factor of 2.1 on the average.

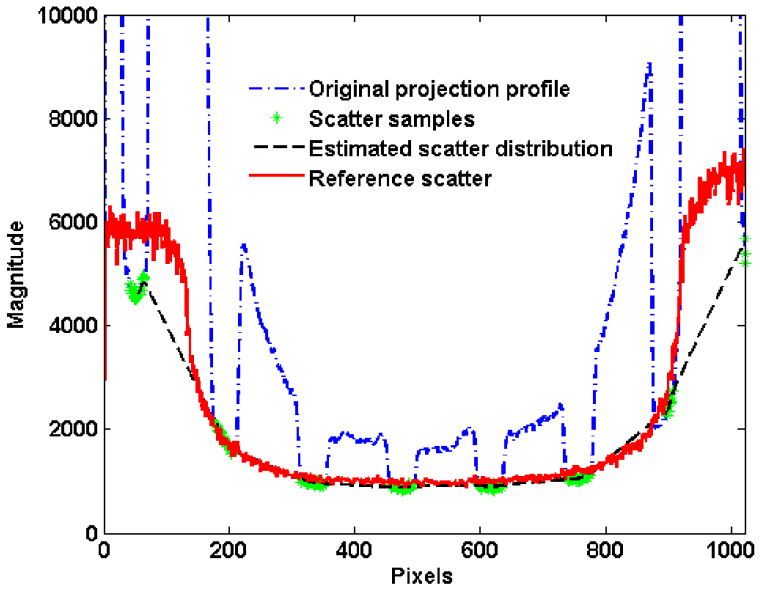

(a)

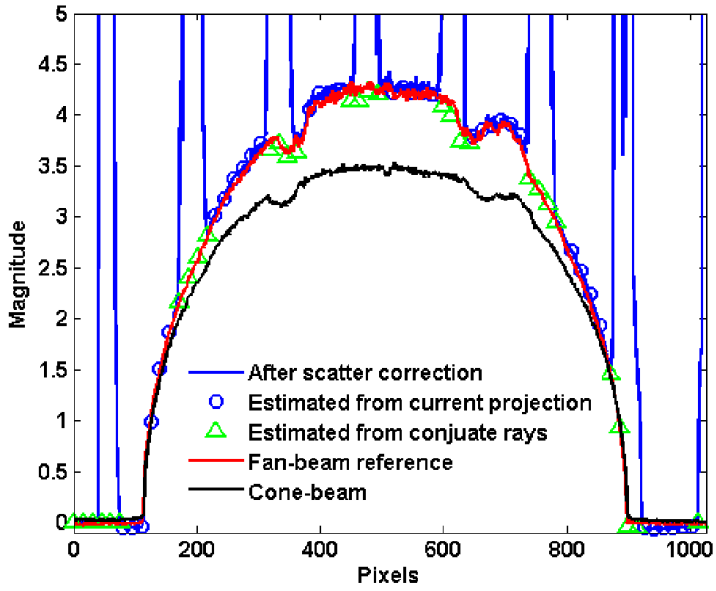

(b)

Figure 2.3 1D horizontal profiles of the scatter, projection and line integral signals acquired from the Catphan©600 phantom: (a) estimated and reference scatter, original projection signals; (b) line integrals of CBCT projections with and without the proposed correction and with a fan-beam geometry. Different markers are plotted to demonstrate the data acquired from direct measurement (circle) and primary compensation (triangle).

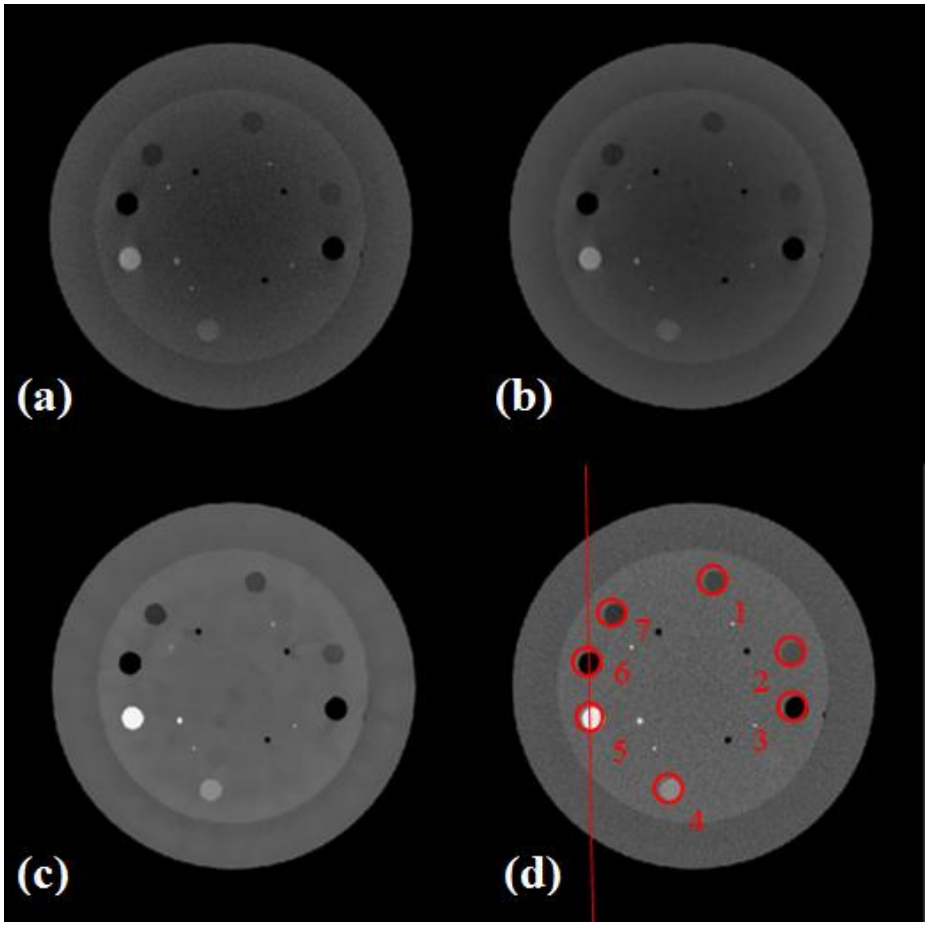

Figure 2.4 Axial views of the reconstructed Catphan©600 phantom. (a) CBCT without scatter correction using FBP algorithm and 655 projections; (b) low–dose CBCT without scatter correction using ABOCS and 163 projections (estimated 75% dose reduction); (c) CBCT using the proposed scatter correction and ABOCS reconstruction using 219 projections (estimated 75% dose reduction); (d) fan-beam CT as the ground-truth using FBP reconstruction and 655 projections. The selected uniform ROIs are marked with red circles in (d). Display windows: [-400 600] HU.

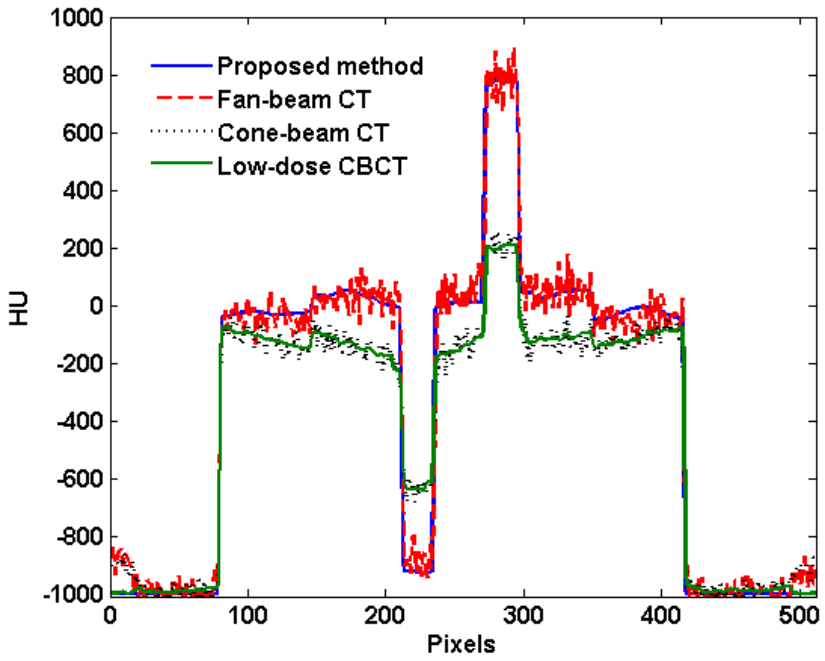

Figure 2.5 Comparison of 1D profiles of the CT images in Figure 2.4, taken along the straight line in Figure 2.4 (d).

Table 2.1 Comparison of the averaged CT numbers and contrasts inside the contrast rods of the Catphan©600 phantom. The CT number errors are also shown in parentheses. The numbers of the ROIs are marked in Figure 2.4 (d). All unites are in HU.

	ROI	1	2	3	4	5	6	7	RMSE
CT #	Fan-beam CT	-131	-84	-895	248	776	-889	-211	
(HU)	CBCT with correction	-148	-107	-933	227	780	-921	-234	
		(-17)	(-23)	(-38)	(-21)	(4)	(-32)	(-23)	24
	CBCT without correction	-239	-217	-646	-48	202	-639	-281	
		(-108)	(-133)	(249)	(-296)	(-574)	(250)	(-70)	250
	CT # improvement	91	110	211	275	570	218	47	
Contrast	CBCT with correction	169	118	934	201	753	933	253	
(HU)	CBCT without correction	88	55	452	112	322	456	126	
	Contrast improvement	1.93	2.13	2.07	1.79	2.34	2.05	2.02	

2.3.3 Anthropomorphic head phantom results

Figure 2.6 shows the axial views of the reconstructed head phantom images using the conventional FBP reconstruction, the low-dose ABOCS reconstruction, and the proposed method. The full-scan fan-beam CT image is generated as the ground-truth. Similar to the Catphan©600 phantom results, the shading artifacts in Figure 2.6 (a) and (b) are significantly suppressed with the proposed method. The mean CT number error is

reduced from over 220 HU (Figure 2.6 (a) and (b)) to 10 HU (Figure 2.6 (c)) in the central uniform area as indicated by the white circle in Figure 2.6 (d). The overall image uniformity of our result (Figure 2.6 (c)) is close to that in the fan-beam result (Figure 2.6 (d)), with only 25% radiation dose of a routine CBCT scan. The comparison of 1D profiles passing through the central horizontal line, as indicated by the red line in Figure 2.6 (d), is shown in Figure 2.7.

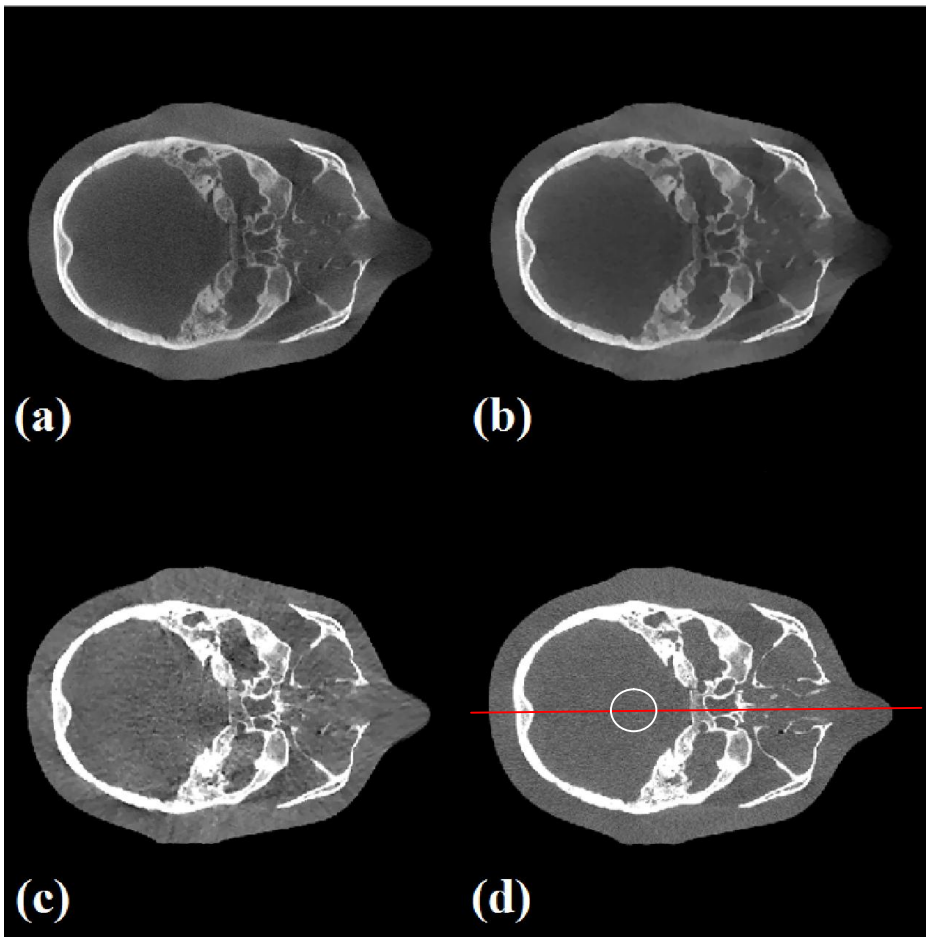

Figure 2.6 Axial views of the reconstructed head phantom. (a) CBCT without scatter correction using FBP algorithm and 655 projections; (b) low–dose cone-beam CT without scatter correction using ABOCS algorithm and 163 projections (estimated 75% dose reduction); (c) CBCT using the proposed scatter correction and ABOCS reconstruction with 219 projections (estimated 75% dose reduction); (d) fan-beam CT using FBP reconstruction and 655 projections. Display windows: [-500 900] HU.

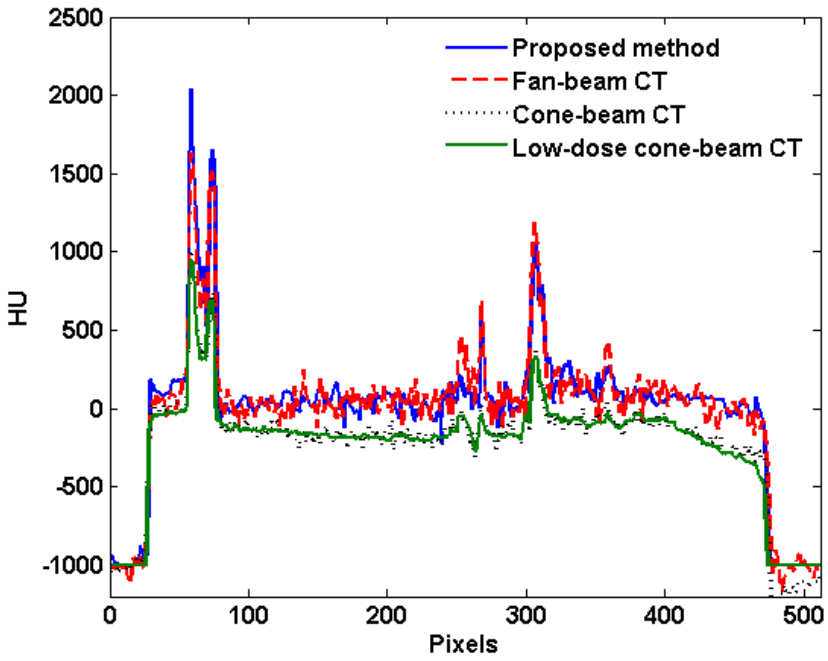

Figure 2.7 Comparison of 1D profiles along the central horizontal line as shown in Figure 2.6 (d).

2.4 Conclusion and discussions

In this work, a practical CBCT imaging method for dose reduction and scatter correction using a stationary blocker in a single scan is proposed. In the tabletop phantom studies, our method reduces the overall CT number error from over 220 HU to less than 25 HU, and increases the image contrast by a factor of 2.1 in the selected ROIs with only 25% dose of a conventional CBCT scan.

For demonstration purposes, only 2D images are reconstructed in this work. In the future, the author will extend our method to 3D reconstruction. Due to the huge size of system matrix, it is not practical to store the whole matrix in the computer memory for iterative CT reconstruction. Instead, the multiplication of system matrix will be

formulated as a forward projection operation and speed up the calculation using hardware acceleration technique, e.g., on a graphics processing unit (GPU) [54, 102]. The other issue with the 3D extension is that the cone angle can be as large as 6° in the off-planes of the OBI system [18], which makes the small cone-angle approximation less accurate. Nevertheless, the artifacts stemming from a large cone angle are generic issues in circular CBCT [103, 104]. For example, the small-cone-angle approximation is also used in 3D FDK reconstruction [95], the current standard algorithm implemented on commercial systems. For the applications of scatter correction with reduced projection measurement, previous studies have shown that the enlarged cone angle leads to negligible image quality degradation on clinical CBCT systems [81]. A similar performance of off-plane imaging is expected with the proposed method in this work. Low-frequency artifacts can be observed on the scatter-corrected images, which result from the insertion of the beam blocker. In the future, we will look into other possible blocker designs to suppress these artifacts.

CHAPTER 3

COMBINED ITERATIVE RECONSTRUCTION AND IMAGE-DOMAIN DECOMPOSITION FOR DUAL ENERGY CT USING TOTAL-VARIATION REGULARIZATION

3.1 Introduction

Since the development of the dual-energy imaging theory [59], dual-energy CT (DECT) has been increasingly used for its capabilities of material decomposition and energy-selective imaging. Due to its advantages on differentiating materials that are indistinguishable on conventional CT images, DECT has shown great promises on more accurate diagnosis for different disease sites, including head and neck [105-107], thoracic [108, 109], cardiac [110] and abdomen [111-113]. One generic problem of current DECT, however, is that the signal decomposition process is unstable, leading to severe noise boost in the resultant images [50, 68, 114, 115] . The purpose of this study is to propose an iterative approach that combines the reconstruction and the signal decomposition procedures to minimize the DECT image noise without noticeable resolution loss.

In the diagnostic energy range, the linear attenuation coefficient of any material can be approximated as a weighted summation of two different actual or even virtual materials, referred to as basis images [59, 60]. In DECT, two CT scans with different spectra are performed on the same object so that the basis images can be computed from the measured projections by solving an inverse problem. The inversion process is referred to as decomposition, which is implemented with either a linear model typically on the image data [117, 118], or a nonlinear model on projection data [116]. Since the linear decomposition model is easy to implement, and also capable of providing material decomposition information, it is more commonly used in clinical environment. This study is focused on DECT with image-domain decomposition.

In DECT, the estimated compositions of materials are mainly determined by the signal difference of the two CT scans. The decomposition, therefore, involves signal cancellation [115]. On the other hand, the noise of the two CT datasets is independent. The direct decomposition reduces signal magnitude and propagates image noise, leading to significantly degraded signal-to-noise ratios (SNR) on resultant images [50, 64, 68, 114]. Many methods have been proposed in the literature to improve the SNR of DECT images. Based on whether noise suppression is performed during reconstruction, these methods are divided into two categories. The first type typically suppresses noise of the reconstructed images of basis materials as an auxiliary step independent from the signal decomposition. A smoothing filter can be applied before or after the image reconstruction, with noise suppressed at the cost of reduced spatial resolution [114, 119, 120]. For example, Macovski *et al.* proposed a sophisticated noise suppression technique, which reduces image noise via low-pass filtering on the selective image and restores the structure information via high-pass filtering on the non-selective image [115, 121]. Researchers also proposed noise suppression techniques based on the statistics of x-ray projections and/or CT images. Kalender *et al.* developed a novel noise suppression technique by implicitly assuming exact negative linear correlation on the noise of decomposed images [50]. The method alleviates the problem of spatial resolution loss compared to the filtering methods, with increased computation time and edge artifacts. The other category of algorithms suppresses image noise by incorporating the decomposition into the reconstruction process. Zhang *et al.* and Fessler *et al* applied a model based iterative reconstruction algorithm which combines the decomposition and reconstruction [122, 123]. An edge-preserving regularization is often included in the formulation to suppress the noise while maintaining the spatial resolution [123]. Recently, Compressed sensing (CS) reconstruction algorithms, including iterative reconstruction using total-variation (TV) regularization, show promise in recovering faithful signals with superior SNR from noisy projection data [53, 75, 117, 124]. The TV regularization

method proposed in this study combines the reconstruction and decomposition steps of DECT in order to minimize the noise propagation during the signal decomposition without significant loss of high-frequency information. The proposed algorithm is formulated as an optimization framework, which balances the data fidelity of CT reconstruction and TV of decomposed images, and the decomposition step is carried out iteratively. The noise in the CT images reconstructed by the proposed algorithm becomes well correlated even though the noise of the raw projections is independent on the two CT scans. Due to this feature, the proposed algorithm avoids noise accumulation during the decomposition process and well preserves the image spatial resolution. The method performance is evaluated on the Catphan©600 phantom and an anthropomorphic head phantom.

3.2 Method

3.2.1 Noise propagation in image decomposition of DECT

In the image-domain decomposition with a linear model, the linear attenuation coefficient of a CT image is approximated as a weighted summation of two images of basis materials [117], i.e.:

$$\begin{pmatrix} x_{H,i,j} \\ x_{L,i,j} \end{pmatrix} = \begin{pmatrix} x_{1H} & x_{2H} \\ x_{1L} & x_{2L} \end{pmatrix} \begin{pmatrix} d_{1,i,j} \\ d_{2,i,j} \end{pmatrix} \qquad \text{Equation 3.1}$$

where $x_{H/L}$ is the reconstructed CT image at high or low tube energies in the unit of mm^{-1}, $d_{1/2}$ is the basis material image (or the decomposed image) and unitless, and i, j are the image pixel indices. The composition matrix consists of elements, $x_{kH/L}$ (k =1 or 2), which are the CT values of basis material measured at high and low tube energies. Conventional methods obtain decomposed images from the two CT scans via direct matrix inversion, i.e.:

$$\begin{pmatrix} d_{1,i,j} \\ d_{2,i,j} \end{pmatrix} = \begin{pmatrix} a & b \\ c & d \end{pmatrix} \begin{pmatrix} x_{H,i,j} \\ x_{L,i,j} \end{pmatrix} = \frac{1}{x_{1H}x_{2L} - x_{2H}x_{1L}} \begin{pmatrix} x_{2L} & -x_{2H} \\ -x_{1L} & x_{1H} \end{pmatrix} \begin{pmatrix} x_{H,i,j} \\ x_{L,i,j} \end{pmatrix}$$

Equation 3.2

where, *a, b, c, d* denote the elements of the decomposition matrix, and $a = x_{2L}/(x_{1H}x_{2L}-x_{2H}x_{1L})$, $b = -x_{2H}/(x_{1H}x_{2L}-x_{2H}x_{1L})$, $c = -x_{1L}/(x_{1H}x_{2L}-x_{2H}x_{1L})$, $d = x_{1H}/(x_{1H}x_{2L}-x_{2H}x_{1L})$.

Equation 3.2 results in severely degraded SNRs on the decomposed images. The reason is two-fold. $x_{kH/L}$ is always positive since it represents the attenuation coefficient of basis material. The elements in each row of the decomposition matrix have opposite signs, i.e. $a \cdot b < 0$, $c \cdot d < 0$. Therefore, the relative magnitude of decomposed images is reduced due to signal cancellation. On the other hand, the noise variance of one pixel on the decomposed images is calculated as,

$$\begin{aligned} \mathrm{var}(n_1) &= a^2 \cdot \mathrm{var}(n_H) + b^2 \cdot \mathrm{var}(n_L) + 2ab\sqrt{\mathrm{var}(n_H) \cdot \mathrm{var}(n_L)}\,\mathrm{corr}(n_H, n_L) \\ \mathrm{var}(n_2) &= c^2 \cdot \mathrm{var}(n_H) + d^2 \cdot \mathrm{var}(n_L) + 2cd\sqrt{\mathrm{var}(n_H) \cdot \mathrm{var}(n_L)}\,\mathrm{corr}(n_H, n_L) \end{aligned}$$

Equation 3.3

where $n_{1/2}$ denotes the noise of the pixel on the decomposed image, and $n_{H/L}$ denotes the noise of the same pixel on the CT image. var(.) calculates the variance and corr(.) calculates the correlation.

If the two CT images are reconstructed independently, their noise correlation is zero. Ignoring the third terms of Equation 3.3, we find that the noise of each decomposed image accumulates from the noise of both CT images. The above two facts jointly lead to reduced SNRs on the decomposed images, which significantly lowers the clinical merits of the direct decomposition approach via matrix inversion.

3.2.2 Combined iterative reconstruction using TV regularization

Equation 3.3 shows that noise in decomposed images can be reduced via noise suppression on CT images. Even if the noise suppression algorithm is applied directly on the decomposed images, an equivalent noise suppression algorithm on CT images for the

same performances can always be obtained, since the decomposition has a one-to-one mapping relationship. To suppress noise in decomposed images, most existing methods, including image filtering [119, 120] and iterative CT reconstruction methods [117], aim to lower the values of the first two terms in Equation 3.3, i.e. to reduce the noise in the reconstructed CT images. These approaches result in inevitable resolution loss due to the general tradeoff between noise suppression and preservation of spatial resolution.

In this work, a distinct method is proposed to suppress noise in decomposed images via reducing the third term in Equation 3.3. The noise in the CT images (i.e. the first two terms in Equation 3.3) is kept as intact as possible to maintain the high spatial resolution of the decomposed images. As $a \cdot b<0$ and $c \cdot d<0$, an equivalent goal is to increase the noise correlation between the CT images. This task is seemingly impossible, since CT image noise of two independent scans is believed to be always uncorrelated. If the two images are jointly reconstructed, the noise correlation of CT images can be increased. An optimization framework is therefore proposed for DECT, which combines the iterative reconstruction of CT images and the decomposition process. The reconstruction of two CT images becomes dependent via the decomposition process performed at each iteration, resulting in increased noise correlation of the final CT images. The algorithm is developed from our previous work on iterative reconstruction for single-energy CT [75]. The proposed optimization framework is formulated as:

$$[x_H^*, x_L^*] = \arg\min[\frac{1}{2}\left\|A\vec{x}_H - \vec{m}_H\right\|_2^2 + \frac{1}{2}\left\|A\vec{x}_L - \vec{m}_L\right\|_2^2 + \beta_1 \cdot R(a\vec{x}_H + b\vec{x}_L) + \beta_2 \cdot R(c\vec{x}_H + d\vec{x}_L)]$$
$$\text{s.t.} x_H \geq 0, x_L \geq 0$$

Equation 3.4

where A is the system matrix that models the forward projection process using Siddon's ray tracing algorithm [125]. $\vec{x}_{H/L}$ is the vectorized reconstructed CT image at high or low energy, and $\vec{m}_{H/L}$ is the vectorized measured projection. R is image regularization term,

and $\beta_{1/2}$ is the weighting on the regularizations of the decomposed images. The commonly used TV is employed as the image regularization term to suppress decomposed image noise and preserve the edges sharpness. For a 2D image, TV of the decomposed images is calculated as,

$$R(d) = \|d\|_{TV} = \sum_{i,j} \left| \vec{\nabla} d_{i,j} \right| = \sum_{i,j} \sqrt{(d_{i,j} - d_{i-1,j})^2 + (d_{i,j} - d_{i,j-1})^2} \qquad \text{Equation 3.5}$$

The proposed algorithm combines reconstruction of CT images at two energies into one framework and applies the regularization on the decomposed images, a distinct feature compared to existing iterative reconstruction algorithms for conventional CT [53, 75, 117, 124]. An equivalent formulation of Equation 3.4 is to use the decomposed images as the control variables in the objective and to apply the regularization directly on the control variables. This formulation, however, may change the computation complexity, since the non-negativity constraint cannot be enforced on the decomposed images.

The quality of image obtained by Equation 3.4 is mainly controlled by the weights on TV regularization, β_1 and β_2. When β increases from a small value, the noise correlation between the two reconstructed CT images increases from 0 towards 1. At the same time, the noise variances of CT images gradually decrease, which is typically accompanied with image blurring artifacts. While both effects contribute to noise reduction on decomposed images (see Equation 3.3), we aim to avoid the latter for preservation of image spatial resolution. In this study, a phantom study is performed to find the range of optimal β values, which produces noise correlation of CT images close to one, while minimally suppresses their individual noise variance. Mathematically, a proper β value depends not only on the data fidelity error but also on the TV value of the true image. For example, β needs to be increased when the image noise increases. Even if the image noise is unchanged, the optimal β value changes for different object geometries due to different TV values.

3.2.3 Implementation details

The proposed algorithm is solved efficiently by gradient projection with an adaptive Barzilai–Borwein (GP-BB) step-size selection scheme which was proposed in our recent publication [75]. The decomposition is to perform a linear transformation on the reconstructed CT images; therefore the combined reconstruction problem is still convex, which guarantees a global solution of the optimization problem. The pseudo code of the proposed combined reconstruction algorithm with TV regularization is shown below. The symbol := means assignment. Both image and data space variables are denoted by a vector sign. N_i is the total number of CT image pixels, which is 512^2 in this study.

$\kappa = 0.3$; $tol = 10^{-9}$ mm^{-1}; $N_{iter} = 100000$;

for i = 1:N_{iter} do

$$\vec{x} := [\vec{x_H}; \vec{x_L}];$$

$$\vec{g} := \begin{bmatrix} A^T(A\vec{x_H} - \vec{m_H}) \\ A^T(A\vec{x_L} - \vec{m_L}) \end{bmatrix} + \begin{bmatrix} \beta_1 \cdot \frac{\partial R(a\cdot\vec{x_H} + b\cdot\vec{x_L})}{\partial \vec{x_H}} + \beta_2 \cdot \frac{\partial R(c\cdot\vec{x_H} + d\cdot\vec{x_L})}{\partial \vec{x_H}} \\ \beta_1 \cdot \frac{\partial R(a\cdot\vec{x_H} + b\cdot\vec{x_L})}{\partial \vec{x_L}} + \beta_2 \cdot \frac{\partial R(c\cdot\vec{x_H} + d\cdot\vec{x_L})}{\partial \vec{x_L}} \end{bmatrix};$$

for l = 1: $2\times N_i$, do

if $g(l) \leq 0$ or $x(l) > 0$, then $p(l):=g(l)$, else $p(l):=0$; end if;

end for;

if{1st iteration}, then

$$\vec{x_{H,old}} := 0;\ \vec{x_{L,old}} := 0;\ \vec{x_{old}} := [\vec{x_{H,old}}; \vec{x_{L,old}}];\ \vec{p_{old}} := 0;\ \alpha := 10^{-8};$$

else

$$\alpha_1 := \frac{(\vec{x} - \vec{x_{old}})^T(\vec{x} - \vec{x_{old}})}{(\vec{x} - \vec{x_{old}})^T(\vec{p} - \vec{p_{old}})}; \alpha_2 := \frac{(\vec{x} - \vec{x_{old}})^T(\vec{p} - \vec{p_{old}})}{(\vec{p} - \vec{p_{old}})^T(\vec{p} - \vec{p_{old}})};$$

If $\alpha_2 / \alpha_1 < \kappa$, then $\alpha := \alpha_1$, else $\alpha := \alpha_2$; end if;

$\overrightarrow{x_{old}} = \vec{x};\ \overrightarrow{p_{old}} = \vec{p};$

end if;

$\vec{x} := \vec{x} - \alpha \vec{p};$

for l = 1: 2×N_i, do

if $x(l)$ <0, then $x(l)$:=0; end if;

end for;

if $\left\| \vec{x} - \overrightarrow{x_{old}} \right\|_2^2 \le tol$

break;

end if;

end for;

$\vec{d}_1 := a\overrightarrow{x_H} + b\overrightarrow{x_L};\ \vec{d}_2 := c\overrightarrow{x_H} + d\overrightarrow{x_L};$

return $\vec{d}_1;\ \vec{d}_2;\ \overrightarrow{x_H};\ \overrightarrow{x_L}.$

3.2.4 Evaluation

The experimental data are taken on our x-ray tabletop system at Georgia Institute of Technology. Projections are acquired at x-ray tube energies of 75 kVp and 125 kVp. Both scans take 655 projections over 360°. The geometry of this system exactly matches that of a Varian On-Board Imager (OBI) CBCT system on the TrueBeam radiation therapy machine. More details of the system setup can be found in our previous publication [81]. To evaluate the performance of the proposed method in the absence of scatter, a fan-beam geometry is used in all the studies [79, 81, 85, 99]. The x-ray beam collimator has a longitudinal width of around 10 mm on the detector for inherent scatter suppression. Therefore, each projection measures a one-dimensional vector of 1024 elements, with a pitch size of 0.388 mm. The size of reconstructed image and decomposed image is 512-by-512, with a pixel size of 0.5-by-0.5 mm^2.

An evaluation phantom, Catphan©600 (The Phantom Laboratory, Salem, NY) and an anthropomorphic phantom are used in our studies. On the Catphan©600 phantom, we first find the range of optimal β values by evaluating our method with different β and investigating its effect on the noise characteristics of the reconstructed CT images. With the optimized β values, the performances of the method on noise suppression as well as other aspects of image quality are assessed. As discussed in detail later, the proposed method is compared with several existing approaches. Since these methods use different frameworks of signal processing, the relative noise levels on the two decomposed images are different as well. It is difficult to obtain the same ratio of noise magnitudes on decomposed images in the comparison of different methods. The average noise standard deviation (STD) of the decomposed images is used to quantify the noise level achieved by each method. The slices of line pairs and contrast rods on the Catphan©600 phantom are used for studies of spatial resolution and decomposition accuracy, respectively. In particular, two vials of iodine solutions with different concentrations, 5 mg/ml and 10 mg/ml, are inserted into the contrast module of Catphan©600 phantom to simulate the diluted iodine solution in patient veins [126]. This study mimics the clinical scenario of contrast-enhanced CT scans, and DECT is used to obtain iodine/bone separation [64, 127]. The errors of electron density on the contrast rods are used as the quality metric of decomposition accuracy. The electron density distribution is calculated from the decomposed images, and compared to the values of ground-truth provided in the Catphan©600 phantom manual. The "true" electron densities of the iodine solutions are calculated based on their iodine concentrations. The estimation error of electron density is calculated as the root of the mean square error (RMSE):

$$\text{RMSE}=\sqrt{\frac{1}{N_{ROI}}\sum_{i=1}^{N_{ROI}}\left(\frac{e_i-\bar{e}_i}{\bar{e}_i}\right)^2}\times 100\% \qquad \text{Equation 3.6}$$

where i is the index of ROI and e_i is the estimated electron density inside the ROI. $\bar{e_i}$ is the ground-truth value, and N_{ROI} is the total number of ROIs. Finally, the proposed method is evaluated on an anthropomorphic head phantom with complex structures.

Our approach is compared with both direct and iterative decomposition methods. The direct decomposition (i.e. Equation 3.2) is performed on the FBP reconstruction without and with apodization (i.e. by applying a Hamming window in ramp filtration with a cutoff frequency) and a CS-based iterative reconstruction [75]. The CS-based iterative reconstruction algorithm was previously developed in our group and referred to as the accelerated barrier optimization for compressed sensing (ABOCS) reconstruction. ABOCS minimizes the image TV term with data fidelity and non-negativity constraints, and the optimization is solved using the GP-BB method in a similar way as described in section 2.3 [75]. The proposed method is also compared with iterative decomposition approaches using the combined iterative reconstruction framework as shown in Equation 3.4 but with different forms of regularization, including quadratic and q-generalized Gaussian Markov random field (q-GGMRF) regularizations [123, 128, 129]. The q-GGMRF regularization term is written as:

$$R\left(\vec{x}\right)=\sum_{\{i,k\}\in C} b_{i,k}\rho\left(x_i-x_k\right) \qquad \text{Equation 3.7}$$

where $b_{i,k}$ are directional weighting coefficients defined as the inverse of the distance between the center pixel i and the elements k in its neighborhood. The potential function $\rho(\Delta)$ is given by:

$$\rho(\Delta)=\frac{|\Delta|^p}{1+|\Delta/c|^{p-q}} \qquad \text{Equation 3.8}$$

where Δ is the adjacent pixel value difference, and constant c determines the approximate threshold of transition between low and high contrast regions. Constants p and q determine the powers near and distant from the origin, respectively. Note that, the

quadratic regularization term is a special case of Equation 3.8 with p=q=2. In this work, the two noise suppression methods are implemented by replacing the regularization term in our algorithm (Equation 3.4) with Equation 3.7 and choose p=2.0, q=1.2, c=10.0 as suggested in Ref. [128] for the q-GGMRF scheme and p=q=2 for the quadratic regularization.

To speed up the calculation, the evaluated algorithms are implemented on an Amax GPU workstation (www.amax.com) using CUDA C (NVIDIA, Santa Clara, CA) to utilize the massive parallel computational capability of the GPU. A single TESLA C2075 card is installed on the workstation, which consists of 448 processing cores with 1.15 GHz clock speed and 6 GB memory.

To evaluate the performance of retaining spatial resolution using different noise suppression schemes, the modulation transfer function (MTF) is calculated using the image region around a steel wire (with a diameter of 0.15 mm) on Catphan©600 phantom. As described earlier in the work, our algorithm achieves a superior performance on noise suppression via increasing noise correlation of CT images. To support the argument, the noise correlation on the reconstructed CT images is calculated:

$$corr = \frac{E[(x_H - E(x_H))(x_L - E(x_L))]}{\text{std}(x_H)\cdot\text{std}(x_L)} \qquad \text{Equation 3.9}$$

where E(.) calculates the mean value, and std(.) calculates the standard deviation.

3.3 Results

3.3.1 β selection

Figure 3.1 shows the noise variance and correlation of the CT images of the Catphan©600 phantom (contrast slice) reconstructed by the proposed algorithm with different penalty weights. The basis materials used in this study are iodine and bone (Teflon). A uniform area of the image is used to calculate the noise variance and

correlation. The noise variance of CT images shown in Figure 3.1 is calculated as the average of noise variance on the 75 kVp and 125 kVp CT images. In this study, β_1 and β_2 are set to be the same value for the clarity of illustration. In practical implementations of the proposed algorithm, including other studies presented in this work, β_1 and β_2 have different values. It is seen that as the β value increases, the noise correlation of the two CT images increases toward 1. The noise variance decreases for large β values, indicating possible loss of spatial resolution. To reach a balance between high spatial resolution and strong noise suppression, the optimal values of β_1 and β_2 are chosen in the range of 0.005 to 0.02, where the noise correlation starts to reach 1 (as enclosed by the two dashed lines in Figure 3.1). The β_1 and β_2 values used in the following phantom studies are listed in Table 3.1.

3.3.2 MTF measurement

Figure 3.2 shows the MTF curves obtained by different algorithms. The MTF curves are measured on the Catphan©600 phantom images shown in Figure 3.4 in a later section, around one of the steel wires (indicated by the arrow in Figure 3.4 (a1)). The basis materials used in this study are iodine and Teflon, The proposed method produces better spatial resolution, compared to other methods. The improvement is more significant when strong noise suppression is applied to obtain smaller background noise (Figure 3.2 (a)). The decomposed image value represents the relative weight of basis materials, thus decomposed image as well as its noise standard deviation are unitless.

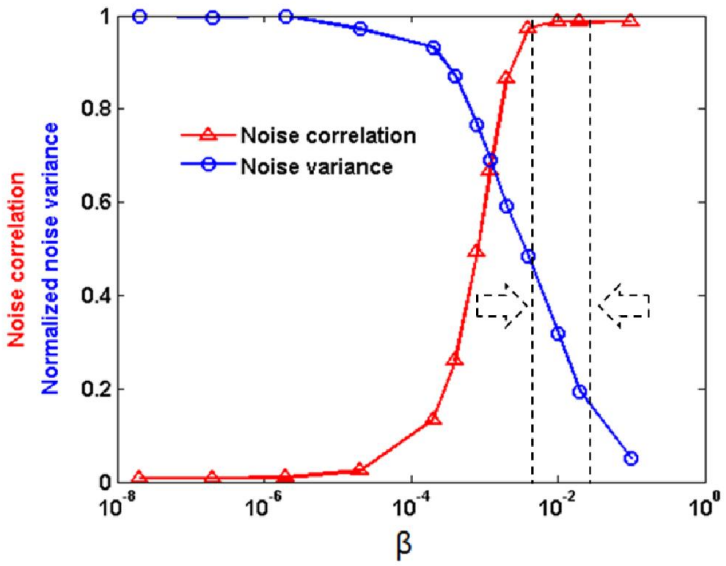

Figure 3.1 Average noise variance of reconstructed CT images using the proposed algorithm and their correlation for different β values. The two dashed lines enclose the area of optimal β values.

Table 3.1 The β values used in the phantom studies

	Catphan slice of line pairs	Catphan slice of contrast rods	Anthropomorphic head phantom
β_1	0.018	0.015	0.006
β_2	0.015	0.010	0.008

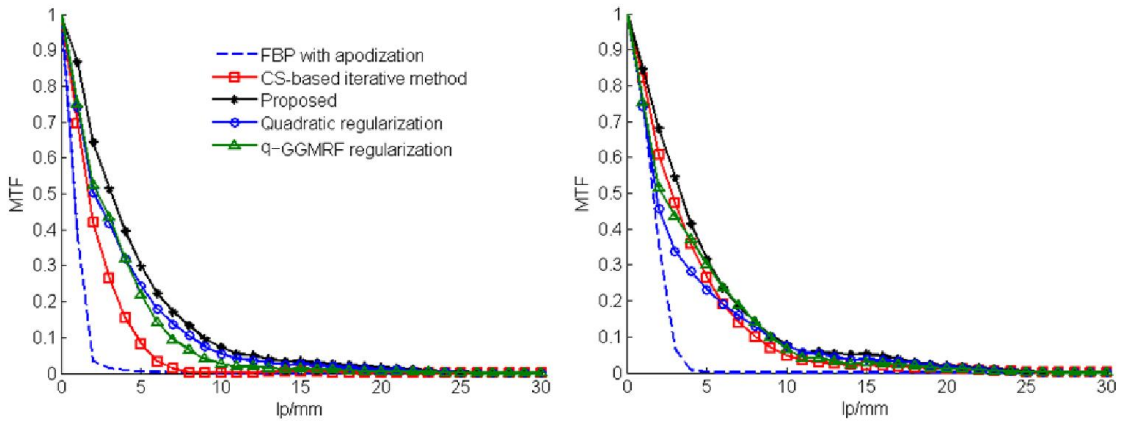

Figure 3.2 MTF curves measured on images generated by different algorithms, including the proposed method, the combined iterative reconstruction method with quadratic and *q*-GGMRF regularizations, and the CS-based iterative reconstruction (ABOCS) and the FBP with apodization followed by direct decomposition. The noise standard deviations are (a) 0.01 and (b) 0.06 on the decomposed image.

3.3.3 Catphan©600 phantom results

Figure 3.3 shows the CT images and the decomposed images of the Catphan©600 phantom on the slice of line pairs using different algorithms. Al and solid water are chosen as the two basis materials of decomposition. The noise STD achieved by one algorithm is calculated as the average of noise standard deviations on the Al and solid water images. Direct decomposition on the FBP reconstruction results in images with excessive noise (see Figure 3.3 (a)). The cut-off frequency of the Hamming window in the ramp-filtration step of the FBP reconstruction (Figure 3.3 (b)) and the penalty weight in the CS-based iterative reconstruction (Figure 3.3 (c)) are adjusted, such that direct decomposition on the CT images reconstructed by these two algorithms achieves the same noise reduction on the decomposed images as the proposed method (Figure 3.3(d)). As seen in the comparison of Al images, especially enlarged images of line pairs, among the images at the same noise level, our algorithm has the best performance on spatial resolution and preserves the structural details contained in the decomposed images with

no noise suppression. This superior performance can be explained by the noise statistics of images, as discussed in section 3.2.1. The correlation of the reconstructed CT images and the noise standard deviation of the decomposed images are summarized in Table 3.2. Apodization and CS-based iterative reconstruction reduces the noise of the CT images by a factor of ~ 30, causing blurs on the CT images. The proposed algorithm generates CT images with noise strongly correlated, and the noise in the decomposed images is significantly suppressed, as shown in Equation 3.3. The strong noise correlation of the high and low energy images is introduced by applying regularization on a linear combination of these images, i.e. the decomposed image. Combined iterative methods with quadratic and *q*-GGMRF regularization both achieve similar noise correlation and spatial resolution around high-contrast objects to TV regularization. However, the proposed TV regularization obtains better edge preservation in the low-contrast region, as shown in Figure 3.3 (d4).

Similar performance of the proposed method is seen in Figure 3.4, the results on the contrast slice of the Catphan©600 phantom. Teflon (with the attenuation similar to bone) and the iodine solution with a concentration of 10mg/ml are used as the basis materials in this study. Similarly, the noise standard deviation achieved by one algorithm is calculated as the average of noise standard deviations on the iodine and Teflon images. All three noise suppression methods reduce the noise standard deviation in the decomposed images by a factor of ~90. The proposed method, however, successfully achieves the highest spatial resolution as demonstrated by the clear visualization of the four small steel wires in the bone image (indicated by the white arrows in Figure 3.4 (e1)). The small wires are excessively smoothed out in the images generated by the other algorithms and cannot be distinguished. Electron densities of the contrast rods measured from the decomposed images and their estimation errors are shown in Table 3.3. All three noise reduction methods obtain slightly more accurate electron density measurement than the FBP without apodization, and our method achieves the best decomposition accuracy.

3.3.4 Anthropomorphic head phantom results

Figure 3.5 shows the CT, the bone and the tissue images of the anthropomorphic head phantom. The average of noise standard deviations on the bone and tissue images is used to quantify the noise performance. Compared to the direct decomposition on the FBP reconstruction, our method reduces the noise standard deviation on the decomposed images by a factor of ~14 while still keeping the spatial resolution of fine structures.

Table 3.2 The noise correlation of CT images, and the noise standard deviation of decomposed images in Figure 3.3. The average noise standard deviations of decomposed images are calculated as the average of Al and water image noise standard deviations inside the solid rectangle (shown in Figure 3.3(a1)).

	Noise correlation	Noise STD
FBP	0.002	0.480
FBP w/ apodization	0.648	0.016
CS-based method	0.669	0.016
Combined method w/ TV	0.997	0.016
Combined method w/ quadratic regularization	0.998	0.016
Combined method w/ q-GGMRF regularization	0.998	0.016

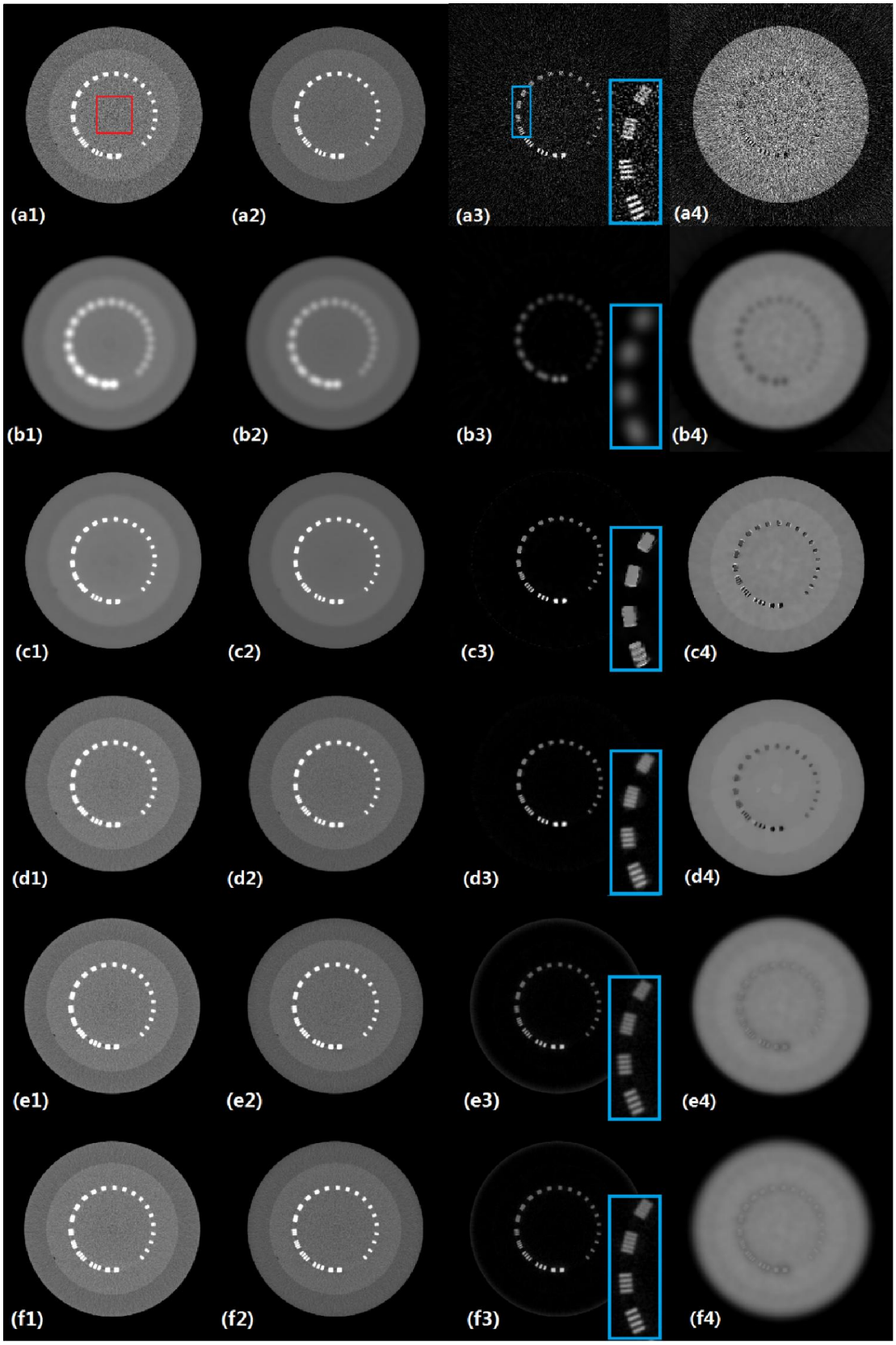
(a1)
(a2)
(a3)
(a4)
(b1)
(b2)
(b3)
(b4)
(c1)
(c2)
(c3)
(c4)
(d1)
(d2)
(d3)
(d4)
(e1)
(e2)
(e3)
(e4)
(f1)
(f2)
(f3)
(f4)

Figure 3.3 CT and decomposed images of the Catphan©600 phantom on the slice of line pairs using (a) FBP and direct decomposition, (b) FBP with apodization and direct decomposition, (c) the CS-based iterative reconstruction and direct decomposition, and (d) the proposed combined iterative reconstruction method with TV regularization (e) the combined iterative reconstruction method with quadratic regularization (f) the combined iterative reconstruction method with *q*-GGMRF regularization. Columns: (1) CT image at 75 kVp, (2) CT image at 125 kVp, (3) Al image (the zoom-in insets show the line pairs) and (4) Water image. Display window: (1-2): [-500 1000] HU, (3): [0 1], (4): [0 2].

Table 3.3 Measurement of electron densities inside the contrast rods of the Catphan©600 phantom. The electron density estimation errors are shown in parentheses. The numbers of the ROIs are marked in Figure 3.4(a1). The ground-truth electron density values of the contrast rods (except the iodine solutions) are obtained from Catphan©600 phantom manual. The electron density of iodine solutions is calculated based on iodine concentrations.

ROI	1 Teflon	2 Delrin	3 Iodine solution (10mg/ml)	4 Polystyrene	5 LDPE	6 PMP	7 Iodine solution (5mg/ml)	RMSE
Ground-truth	6.240	4.525	3.368	3.400	3.155	2.851	3.356	
FBP	6.303	4.963	3.100	3.792	3.569	3.217	3.248	
	(1.0%)	(9.7%)	(8.0%)	(11.5%)	(13.1%)	(12.8%)	(3.2%)	9.5%
FBP w/ apodization	6.045	4.722	3.105	3.680	3.464	3.204	3.171	
	(3.1%)	(4.4%)	(7.8%)	(8.2%)	(9.8%)	(12.4%)	(5.5%)	7.9%
CS-based iterative reconstruction	6.076	4.745	3.064	3.655	3.429	3.170	3.089	
	(2.6%)	(4.9%)	(9.0%)	(7.5%)	(8.7%)	(11.2%)	(8.0%)	7.9%
Proposed	6.271	4.778	3.605	3.606	3.432	3.178	3.521	
	(0.5%)	(5.6%)	(7.0%)	(6.1%)	(8.8%)	(11.5%)	(4.9%)	7.1%

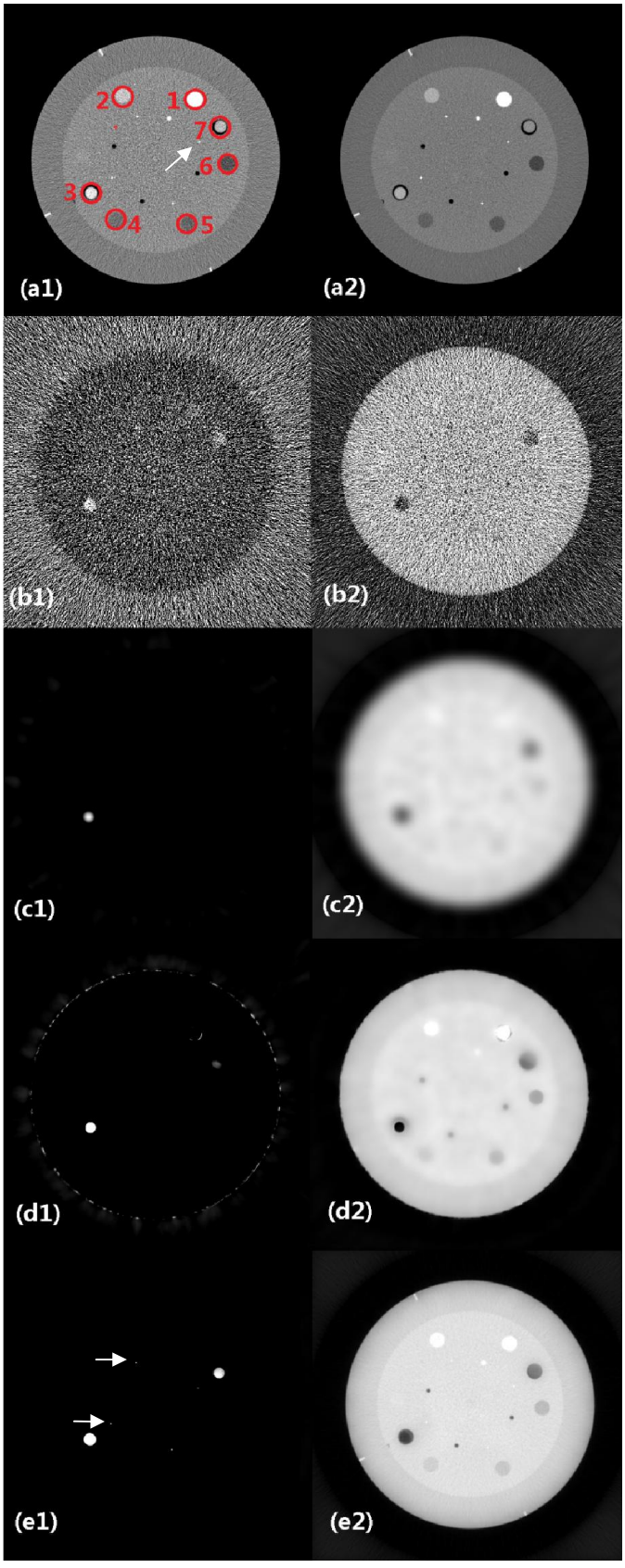
2
1
7
6
3
4
5
(a1)
(a2)
(b1)
(b2)
(c1)
(c2)
(d1)
(d2)
(e1)
(e2)

Figure 3.4 Results of the Catphan©600 phantom on the slice of contrast rods. CT images (a1) at 75 kVp, (a2) at 125kVp and decomposed images of Catphan©600 phantom using (b) FBP and direct decomposition, (c) FBP with apodization and direct decomposition, (d) the CS-based iterative reconstruction and direct decomposition, and (e) the proposed method. (b1-e1) decomposed Iodine image, (b2-e2) decomposed bone (Telfon) image. The arrows in (e1) indicate the small objects that are preserved by the proposed method. The arrow in (a1) indicates the dot object used in the MTF measurements shown in Figure 3.2. The average noise STDs of decomposed images (calculated as the average of iodine and bone image noise standard deviations) are (b) 1.11, (c) 0.012, (d) 0.012, (e) 0.012. Display window (a): [-500 700] HU, (b1-e1): [0 0.2], (b2-e2): [0 1].

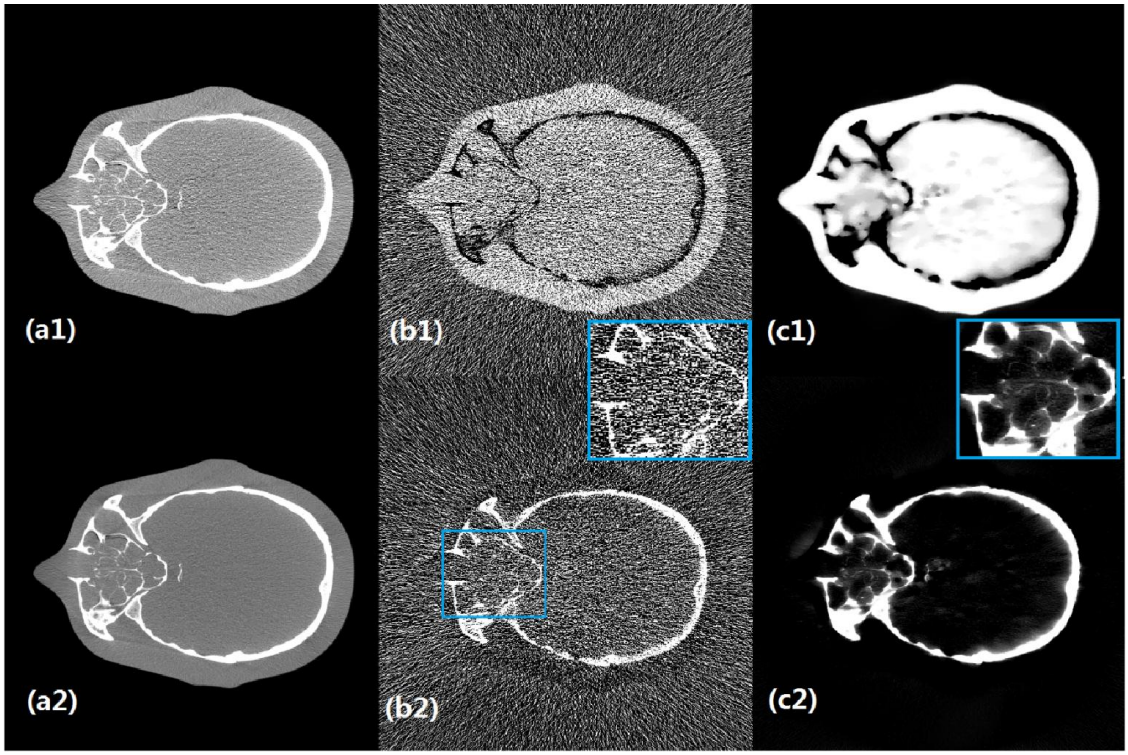

Figure 3.5 Results on the anthropomorphic head phantom. CT images (a1) at 75 kVp, (a2) at 125kVp and decomposed images of the head phantom using (b) FBP and direct decomposition, (c) the proposed method. (b1-c1) decomposed tissue image, (b2-c2) decomposed bone image. The zoom-in bone images of the nasal area are shown as insets. The box in (b2) indicates where the zoom-in images are taken. The average noise standard deviation of decomposed images (calculated as the average of bone and tissue image noise standard deviations) are (b)1.30, (c) 0.09, Window level (a): [-500 700] HU, (b)&(c): [0 1].

3.4 Conclusion and discussions

An algorithmic approach to suppress noise of DECT images is proposed in this study. The algorithm combines iterative reconstruction and material decomposition into one optimization framework. Although the projection data are taken in two independent scans, the noise of the two CT images reconstructed by the proposed method becomes strongly correlated. This feature endows the method an attractive capability of significant noise suppression on the decomposed images. Phantom results show that our method achieves superior performance on DECT imaging, with respect to decomposition accuracy, noise reduction and spatial resolution. A side effect of the improved correlation of the CT images, however, is that measurement errors in one CT scan may be introduced into the other dataset of CT scan. The CT images reconstructed by the proposed algorithm share a similar pattern of artifacts.

Future work is needed to further improve the performance of our method. The design of the proposed iterative algorithm is inspired from the CS-based iterative CT reconstruction algorithms. The combination of CT reconstruction and image decomposition increases the computational complexity of the problem and the algorithm takes a large number of iterations to converge (around 20,000-50,000 in our implementations). Different approaches will be investigated to improve the convergence of the algorithm. Despite low noise, the decomposed images obtained by our method show residual errors, especially around dense objects. The accuracy of electron density measurement also needs improvements. A major source of these errors is the linear model used in the image-domain decomposition method. The beam-hardening effects stemming from the poly-energetic spectrum of the x-ray source are more precisely described by a non-linear formulation. Projection-domain methods based on non-linear models therefore obtain more accurate decomposition [116, 130]. Projection-domain decomposition will be implemented to improve the algorithm. However, the method design could be

complicated due to the nonlinearity of the signal processing. Finally, the proposed method is based on the same physical principle of the conventional DECT, and therefore has similar requirements on the data acquisition. For example, it requires an exact alignment of geometries in the low and high energy scans.

CHAPTER 4

A GENERAL FRAMEWORK OF NOISE SUPPRESSION IN MATERIAL DECOMPOSITION FOR DUAL-ENERGY CT

4.1 Introduction

In Chapter 3, we propose a combined iterative reconstruction and decomposition method for noise suppression in DECT. However, this method employs a linear decomposition model, which does not exploit the benefit of dual energy CT on beam-hardening correction. Furthermore, the combined method implements the reconstruction process iteratively, which is computational intensive. In this chapter, we propose a general framework of iterative noise suppression algorithms for DECT, which uses non-linear decomposition for beam-hardening correction, and avoids reconstruction in the de-noising process to speed up the calculation.

A critical procedure of DECT is the signal decomposition from two sets of projection data acquired at two different x-ray spectra. The raw projections are converted into line integrals of basis materials (e.g. soft tissue and bone) using an analytical or numerical decomposition function, which is either measured during system calibration [133] or estimated using x-ray spectrum simulation [134]. For DECT in the diagnostic energy range, the decomposition function is non-linear in nature, but with a dominant linear component. The decomposed CT images are reconstructed from the line integrals of basis materials using CT reconstruction algorithms. In general, the decomposition step cannot commute with the reconstruction in the signal processing chain, due to its non-linearity. If the decomposition function is approximated as linear and a linear reconstruction algorithm (e.g. the standard filtered back-projection (FBP) reconstruction) is used, the projection-domain decomposition plus reconstruction of decomposed material images is equivalent to the conventional CT reconstruction followed by linear image-

domain decomposition. Such an image-domain decomposition approach has an advantage of directly operating on conventional CT images. It is therefore considered to be more convenient on clinical CT scanners, where raw projections are not always readily extractable for advanced users. Nonetheless, by ignoring non-linear components in the decomposition function, the image-domain decomposition methods cannot correct for beam-hardening errors and therefore do not fully gain the benefits of DECT on energy-selective imaging.

The signal decomposition of DECT implemented on clinical CT systems is very sensitive to the noise in the two sets of dual-energy projection data, since the distributions of linear attenuation coefficients of basis materials have significant overlapping in the diagnostic x-ray energy range [132]. The decomposed images therefore have severely degraded signal-to-noise ratios (SNR), which entails prominent dose increase on the CT scans to retain the clinical values of DECT. Many methods have been proposed in literature to alleviate the noise boost problem [50, 114, 115, 135], and they have been reviewed in Chapter 3 of this dissertation. These existing algorithms suppress image noise either before or after the decomposition, and do not fully explore the statistical properties of the decomposition process. We have previously developed an iterative decomposition method for DECT [131]. The method combines the noise suppression and material decomposition into an iterative process and achieves both goals simultaneously. Using a formulation of best linear unbiased estimator, we estimate the full variance-covariance matrix of the decomposed images and achieve superior performance on noise suppression of DECT without losing image spatial resolution. Nonetheless, a linear model is used for the decomposition function in the previously proposed method. Although the computation is greatly simplified and the decomposition is conveniently performed in the image domain, the algorithm lacks the capability of beam-hardening correction from non-linear decomposition and thus loses one main advantage of DECT.

In this work, we expand the previously developed iterative algorithm to include a non-linear decomposition model for noise suppression in DECT. The method is formulated as a general framework of optimization, with no assumptions on the decomposition functions. A general form of the noise variance-covariance matrix, which is directly calculated from the measured projections and the decomposition function, is derived for use in the iterative algorithm. As a demonstration of algorithm implementation, we employ an existing method of empirical polynomial fitting for non-linear decomposition in the projection domain [61]. The proposed approach is evaluated using phantom studies, on the performance of noise suppression, spatial resolution and beam-hardening correction.

4.2 Methods

4.2.1 A general framework of noise suppression in DECT

We formulate the noise suppression algorithm in the form of least-square estimation with smoothness regularization. Based on the design principles of a best linear unbiased estimator, we include the inverse of the estimated variance-covariance matrix of the decomposed images as the penalty weight in the least-square term. The regularization term enforces the image smoothness by calculating the square sum of neighboring pixel value differences. The general framework of noise suppression is written as:

$$\min_{x}(\vec{x}-\vec{x}_0)^T W^{-1}(\vec{x}-\vec{x}_0)+\beta R(\vec{x}) \qquad \text{Equation 4.1}$$

where $\vec{x}_0$ is the basis material image reconstructed with FBP from decomposed signals. The decomposition can be carried out using a linear or a non-linear model, in the image or the projection domain. $\vec{x}$ is the basis material image with noise suppression to be estimated. $R(\vec{x})$ is regularization term to enforce the smoothness. β is the weighting on the image regularization. W is the noise variance-covariance matrix of the observations to

be included in the optimization framework based on Gauss–Markov theorem and the design principles of a best linear unbiased estimator [136].

We choose $R\left(\vec{x}\right)$ in the form of quadratic smoothness penalty function that penalizes the square sum of the differences between one pixel and its nearest horizontal and vertical neighbors. The penalty function is defined as:

$$R\left(\vec{x}\right)=\frac{1}{2}\sum_{i}\sum_{k\in N_k} e_{ik}\left(x(i)-x(k)\right)^2 \qquad \text{Equation 4.2}$$

where N_k is the set of the four neighbors of the i-th pixel in the image. e_{ik} is the edge-detection weight, which equals zero if either i or k is the index of an edge pixel in the image and one otherwise. The edges on the CT images can be detected using standard edge detection algorithms, as shown in our previous work [131].

For a superior noise suppression performance, it is critical to include an accurate matrix W in the proposed framework. We have previously derived the matrix W when the decomposition has a simple linear form [131]. In this chapter, we aim to find the calculation formula of W for any general-form decomposition used in DECT.

Denote $p_{H/L}$ as polychromatic CT raw data (line integrals) with high/low x-ray energies, and $l_{1/2}$ as decomposed material line integrals. The decomposition function is written as,

$$l_{1/2}=f_{1/2}(p_H, p_L) \qquad \text{Equation 4.3}$$

As shown in the Appendix, W can be simplified as:

$$W=\begin{pmatrix} w_1\cdot I & w_3\cdot I \\ w_4\cdot I & w_2\cdot I \end{pmatrix} \qquad \text{Equation 4.4}$$

where W has a size of $2N$x$2N$, and N is the number of pixels in decomposed images. We define $n_{H/L}$ as the statistical noise in CT images. var(.) calculates the variance. w_1, w_2, w_3, w_4 are calculated as,

$$w_1 = [\frac{\partial f_1}{\partial p_H}(p_H, p_L)]^2 \text{ var}(n_H) + [\frac{\partial f_1}{\partial p_L}(p_H, p_L)]^2 \text{ var}(n_L)$$

$$w_2 = [\frac{\partial f_2}{\partial p_H}(p_H, p_L)]^2 \text{ var}(n_H) + [\frac{\partial f_2}{\partial p_L}(p_H, p_L)]^2 \text{ var}(n_L)$$

$$w_3 = w_4 = \frac{\partial f_1}{\partial p_H}(p_H, p_L) \cdot \frac{\partial f_2}{\partial p_H}(p_H, p_L) \cdot \text{var}(n_H) + \frac{\partial f_1}{\partial p_L}(p_H, p_L) \cdot \frac{\partial f_2}{\partial p_L}(p_H, p_L) \cdot \text{var}(n_L)$$

4.2.2 Non-linear decomposition of DECT

To correct for the beam-hardening artifacts, we employ an empirical dual energy calibration method, which applies the decomposition on the projection data with a polynomial function [61]:

$$l_{1/2} = f_{1/2}(p_H, p_L) = \sum_{i,j=0,\ldots,N_f} (c_{i,j})_{1/2} p_H^i p_L^j \qquad \text{Equation 4.5}$$

In this study, we find that N_f= 3, third-order polynomial function, is adequate for our data. Therefore, the total number of coefficients $c_{i,j}$ in each decomposition function is 16, which makes 32 unknown coefficients in total.

The empirical dual energy calibration method relies on a calibration phantom that must provide path length variations through two basis materials, and combinations of path lengths through both materials [61]. To get an accurate estimation of the 32 unknown coefficients, we design a calibration phantom, where all the thickness combinations of the two basis materials are measured with one single projection. In this study, we use water and Al as the two basis materials. The phantom is designed as shown in Figure 4.1, where the Al wedge changes its thickness vertically, and the Lucite (solid water) wedge changes its thickness horizontally. The calibration phantom's dimension should be of the same order of magnitude as the test object. For the target application on Catphan and head phantoms, we use BE = 8 cm and AD = 25 cm in our design. The phantom height, AB, is properly set to make full use of the flat-panel detector. The

proposed method is designed for on-board CBCT systems, where the imager-to-source distance is 150 cm. We place the calibration phantom at 75 cm to the source and use AB =15 cm. Four markers, made of lead, are placed between the two wedges to determine the position of the calibration phantom from projections, as seen in Figure 4.1 (b).

With the knowledge of phantom position, we can calculate the line integral of basis material, $l_{1/2}$ in Equation 4.5, via a forward projection technique. With the measured dual energy projections, we generate 16 sinograms whose entries are $p_H^i p_L^j$. Equation 4.5 can be seen as a set of linear functions with 32 unknown variables. With the knowledge of $p_H^i p_L^j$ and $l_{1/2}$, we solve the linear functions with a Matlab-based modeling system for convex optimization, CVX. DECT projection data are decomposed simply through the polynomial function with the pre-calculated 32 decomposition coefficients. The reconstructed basis material images are then synthesized for a given single energy, which is free of beam-hardening artifacts.

Decomposition using Equation 4.5 generates basis material line integrals with dramatically increased noise, thus decomposed image with severely degraded SNR. Similar to image-domain decomposition with a linear model, the estimated compositions of materials with projection-domain decomposition are mainly determined by the signal difference of the two CT scans. And image noise from the two CT scans is propagated and accumulated through the decomposition process. Therefore, the projection-domain decomposition leading to significantly degraded SNR on resultant images.

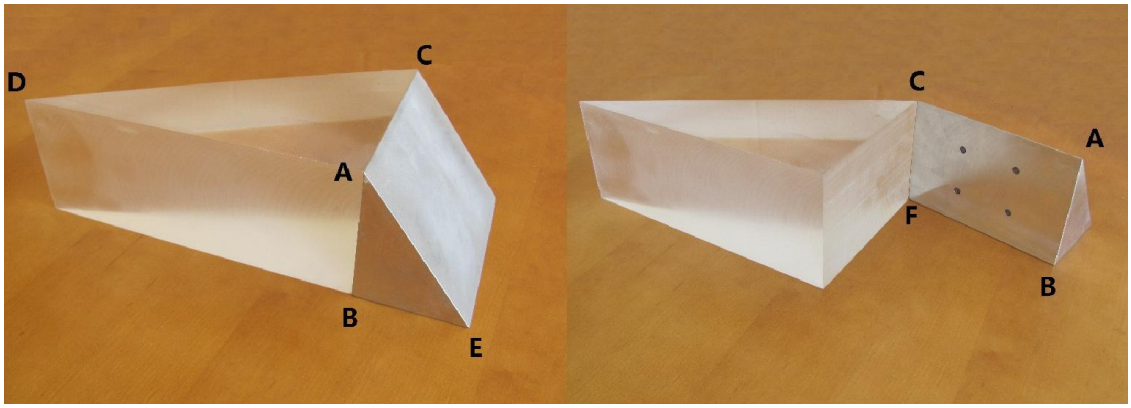

(a) (b)

Figure 4.1 Calibration phantom design. The Al wedge changes its thickness vertically, and the Lucite (solid water) wedge changes its thickness horizontally. Four lead markers are inserted between the two wedges to determine the position of calibration phantom.

4.2.3 Evaluation

All the data were acquired on our tabletop CBCT system at Georgia Institute of Technology. An evaluation phantom, Catphan©600, and an anthropomorphic head phantom are used in our studies. The phantoms were scanned using two x-ray source energies of 125 kVp and 75 kVp, with a tube current of 80 mA and a pulse width of 13 ms. The reconstructed image has a dimension of 512×512 with a pixel size of 0.5×0.5 mm^2.

We first perform a phantom study on the line pair slice of an evaluation Catphan©600 phantom to evaluate the noise suppression performance of the proposed method. The results are compared with those obtained with the conventional formulation of least square estimation with smoothness regularization, i.e.:

$$\min_{\vec{x}}(\vec{x}-\vec{x}_0)^T(\vec{x}-\vec{x}_0)+\beta R(\vec{x}) \qquad \text{Equation 4.6}$$

In the contrast slice of Catphan©600 phantom, we insert six Al rods, and evaluate the performance of the iterative noise suppression scheme with linear and non-linear decomposition methods. On the head phantom, we choose a slice with the sinus

structures to observe the performance of maintaining the spatial resolution. We use noise standard deviation (STD) of a selected uniform region of interest (ROI) and spatial nonuniformity (SNU) as image quality metric. The beam-hardening artifacts caused nonuniformity in the reconstructed image. We measured the SNU as [137],

$$\mathrm{SNU} = \frac{\overline{HU}_{\max} - \overline{HU}_{\min}}{1000} \times 100\% \qquad \text{Equation 4.7}$$

Different ROIs are selected in the CT and synthesized images at both the center and periphery. $\overline{HU}_{\max}$ and $\overline{HU}_{\min}$ in Equation 4.7 are the maximum and the minimum of the mean CT number values of these ROIs.

The penalty parameter, β, was empirically chosen based on a comparable noise variance on the decomposed material images using the proposed. The details of the algorithm implementation is elaborated in [131].

4.3 Results

4.3.1 Catphan©600 phantom results

We first evaluate the performance of the proposed algorithm on maintaining the spatial resolution after material decomposition in the line pair slice. The CT images of the slice are shown in Figure 4.2, and the decomposed images as well as the synthesized monoenergetic images are shown in Figure 4.3. The noise STDs are calculated inside the solid rectangle as shown in Figure 4.3 (a1) and summarized in Table 4.1. Without noise suppression, the non-linear decomposition method results in high noise level in the decomposed images (Figure 4.3 (a2) and (a3)). The STDs are as high as 0.822 and 0.207 in the water and Al images. After iterative noise suppression, the STDs in the two decomposed images are reduced to 0.008 and 0.017, respectively. The noise in synthesized images is also suppressed due to the noise reduction on the decomposed images, where the noise STD is reduced from 230 HU to 61 HU. With the highly reduced noise level, we still keep the high spatial resolution as shown in Figure 4.3 (b2) and (b3).

Under the comparable noise levels, the iterative noise suppression method maintains the spatial resolution of the CT images and outperforms the de-noising scheme with conventional formulation of least square estimation with smoothness regularization (Figure 4.3 (c)). To better visualize the improvement, we enlarge the resolution structures and show the zoom-in displays. As indicated by the white arrows, with proposed method, the line pair can be separated clearly with significant suppressed noise level. The conventional formulation suppresses the image noise on the decompose images as well as synthesized images. However, the line pairs indicated by the white arrow are blurred thus cannot be distinguished.

To evaluate the performance of the iterative noise suppression method with linear and non-linear decomposition, we carry out another study on the Catphan©600 phantom with six Al rods. Figure 4.4 shows the CT images, and Figure 4.5 shows the decomposed images as well as the synthesized images. As shown in Figure 4.4, due to the insertion of Al rods, CT images show severe streaking artifacts resulting from beam-hardening effects. The non-linear decomposition model generates two basis material images, and corrected for beam-hardening artifacts. As seen in Figure 4.5 (a1) and (b1), with non-linear decomposition method, the synthesized images are free of streaking artifacts and is more uniform. Linear decomposition method is also capable of providing material decomposition information, however, cannot correct for beam-hardening artifacts (Figure, 4.5 (c1) and (d1)). Table 4.2 lists the SNU of CT and synthesized images calculated with 11 ROIs indicated by the dashed squares in Figure 4.4 (a). After noise suppression, the SNU error calculated on the synthesized images is decreased from 24.3% with linear decomposition model, to 4.0% with non-linear decomposition model. Note that without noise suppression, the synthesized images show higher level of SNU, since noise also decreases image uniformity.

As listed in Table 4.3, the propose noise suppression method suppress the noise in both decomposed images by one order of magnitude. With both linear and non-linear

decomposition models, the iterative noise suppression method achieves the superior spatial resolution as demonstrated by the clear visualization of the four small steel wires in the Al image as well as the synthesized images, as indicated by the arrows in Figure 4.5.

Table 4.1 The noise STD of the pixel values inside the ROI indicated by the solid rectangle as shown in Figure 4.3 (a1).

Algorithm	Synthesized image	Water image	Al image
Without noise suppression	230 HU	0.822	0.207
Proposed method	61 HU	0.008	0.017
Convectional de-noising	53 HU	0.008	0.017

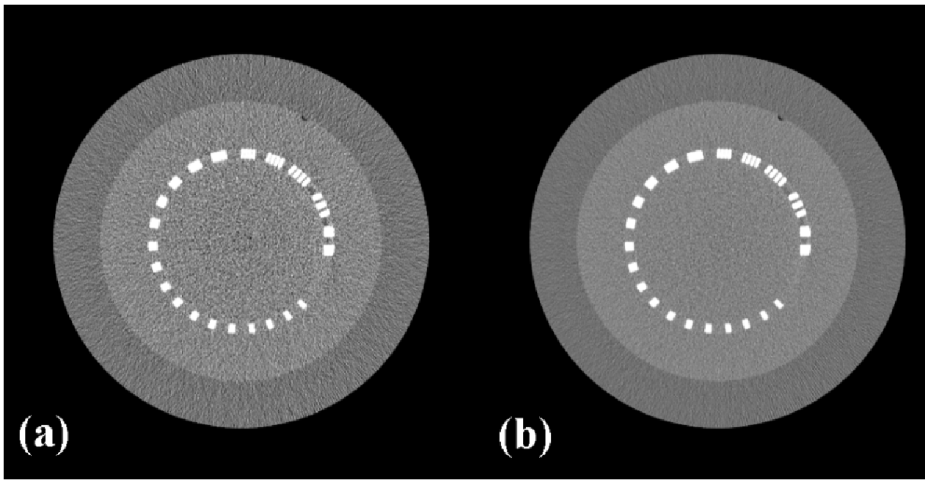

Figure 4.2 CT images of the resolution line pair slice using (a) 75 kVp and (b) 125 kVp tube voltage. Display window: [-500 500] HU.

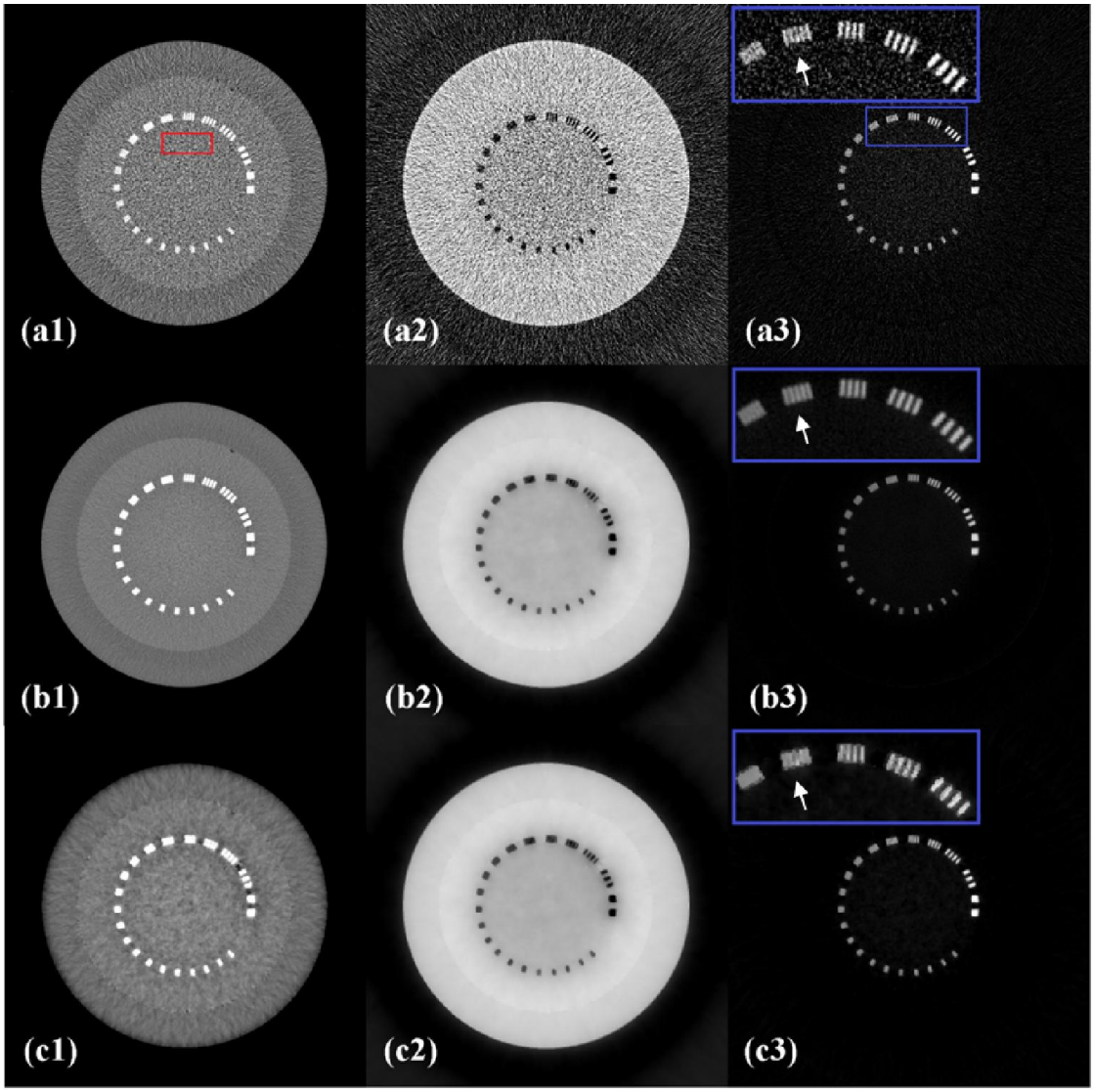

Figure 4.3 Synthesized and decomposed images of the resolution line pair slice (a): without noise suppression; (b): using the proposed iterative noise suppression method; (c): using conventional formulation of least square estimation with smoothness regularization. Column (1): Synthesized image at 74 keV; (2): Al images; (3): Water images. The solid rectangle in (a1) indicates the ROI where the STDs are calculated. Display window: (a) [-500 500] HU; (b-c): [0 1.2].

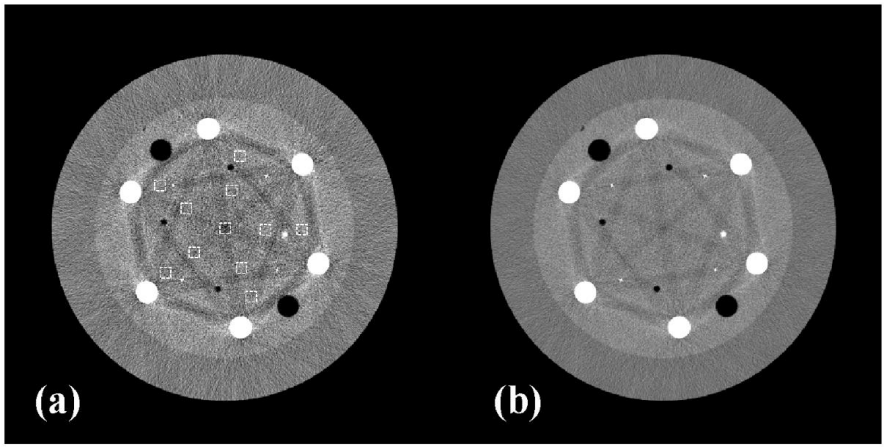

Figure 4.4 CT images of the contrast rods slice using (a) 75 kVp and (b) 125 kVp tube voltage. Display window: [-500 500] HU.

Table 4.2 The SNU of CT and synthesized images. 11 ROIs are selected to calculate the SNU, as indicated by the dashed rectangles as shown in Figure 4.4 (a).

Algorithm	SNU	
75 kVp CT	28.9%	
125 kVp CT	16.4%	
	w/o de-noising	w/de-noising
Non-linear decomposition	11.2%	4.0%
Linear decomposition	39.1%	24.3%

Table 4.3 The noise STD of the pixel values inside the ROI indicated by the solid rectangle as shown in Figure 4.5 (a1). The noise STD of decomposed image is calculated as the average of Al and Water image noise STDs.

Algorithm		Merged image	Decomposed image
Non-linear decomposition	w/o noise suppression	235 HU	0.385
	w/ noise suppression	85 HU	0.019
Linear decomposition	w/o noise suppression	193 HU	1.259
	w/ noise suppression	74 HU	0.019

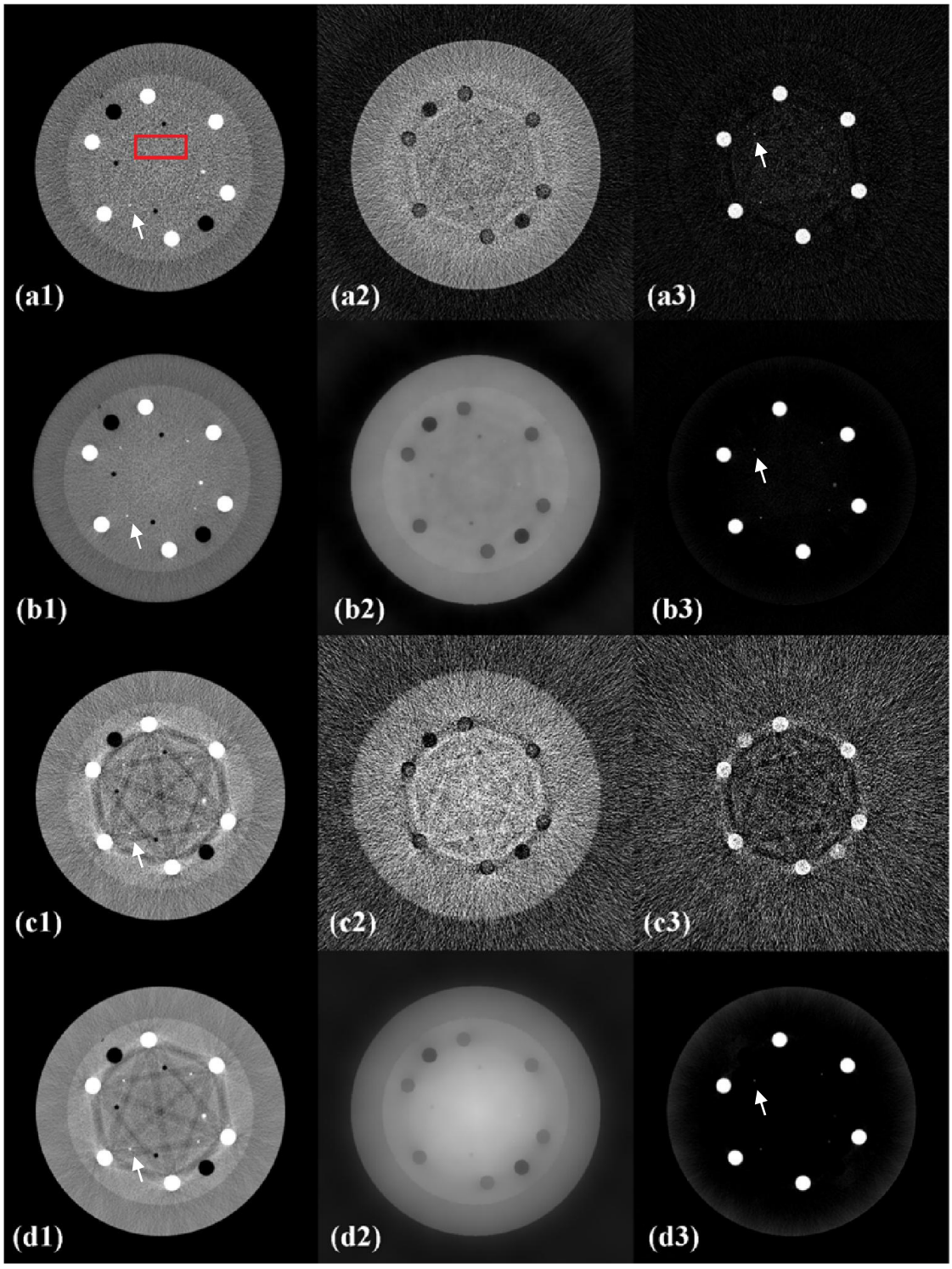

Figure 4.5 Synthesized and decomposed images of the contrast rods slice using (a): non-linear decomposition without noise suppression; (b): the proposed iterative noise

suppression method with non-linear decomposition; (c) linear decomposition without noise suppression; (d) linear decomposition with iterative noise suppression method. Column (1): Synthesized image at 74 keV; (2): Water images; (3): Al images. Display window: (1): [-500 500] HU; (2): [0 2]; (3): [0 0.6].

4.3.2 Anthropomorphic head phantom results

We further carry out a study on an anthropomorphic head phantom with complicated sinus structures. Similar to Catphan results, the non-linear decomposition method suppresses the streaking artifacts resulting from beam-hardening effect, as seen in Figure 4.6 (c). Without noise suppression, the material decomposed images are noisy, and the fine structures in the sinus area are not distinguishable. With the proposed iterative de-noising method, the image noise is suppressed, and these fine structures are clearly visualized in Figure 4.7 (b2). The zoom-in displays are shown in Figure 4.8. The proposed method suppresses the noise by a factor of 22 while maintains higher spatial resolution.

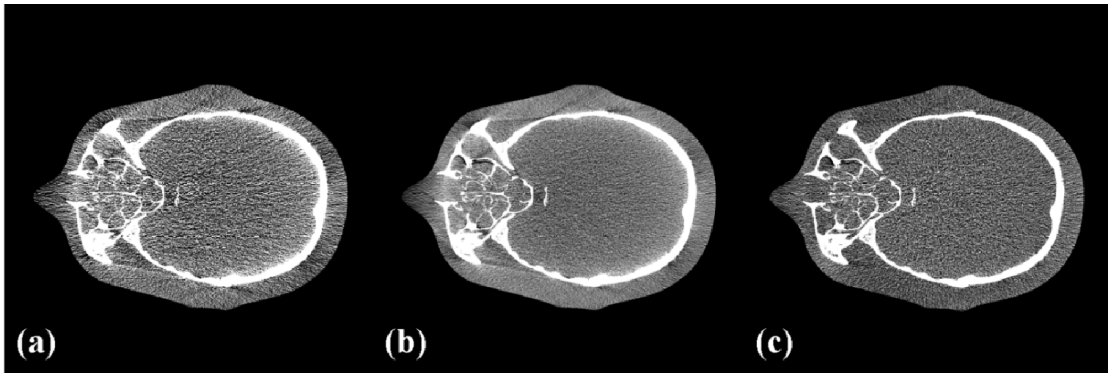

Figure 4.6 CT images of the head phantom using (a) 75 kVp and (b) 125 kVp tube voltage, and (c) merged image at 74 keV. Display window: [-150 200] HU.

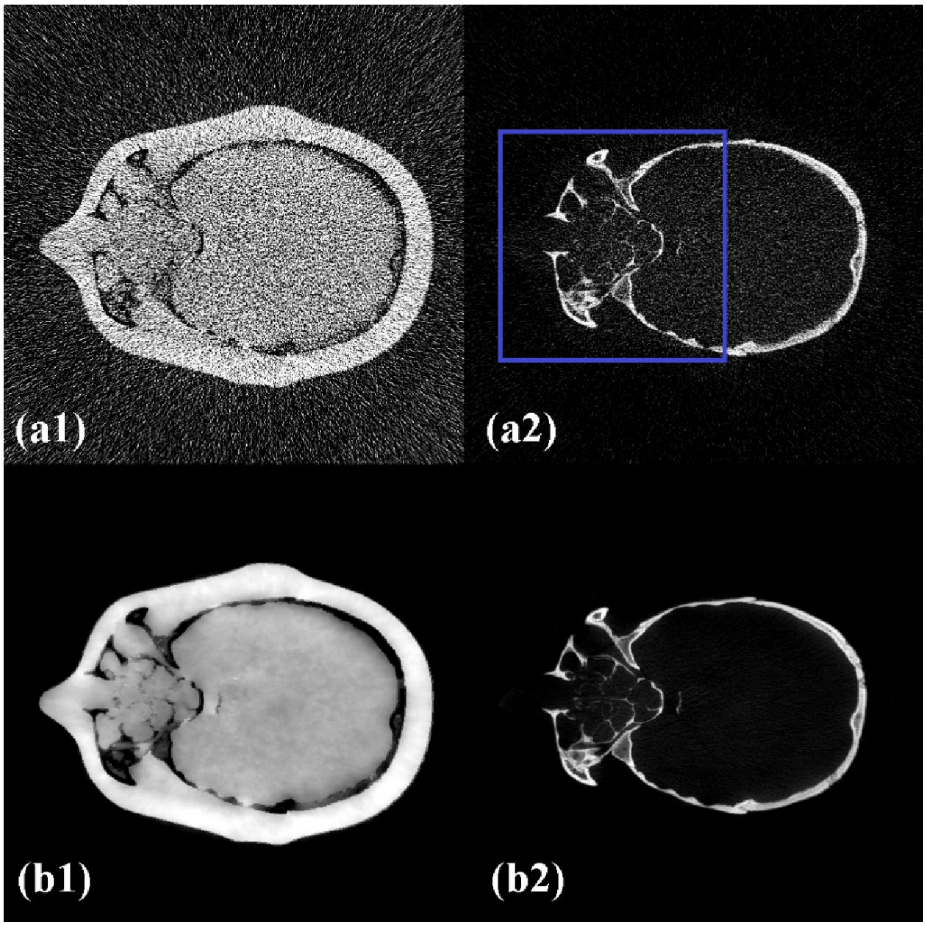

Figure 4.7 Decomposed images of the head phantom. Row (a): without noise suppression; (b): with the proposed iterative noise suppression method. Column (1): water images; (2): Al images. The rectangle indicates the area where the zoom-in displays are shown in Figure 4.8. Display window: [0.1 0.8].

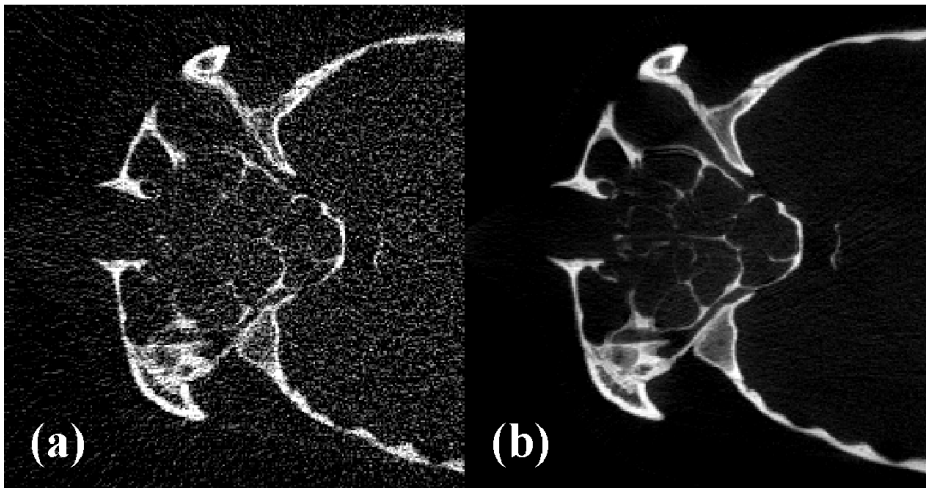

Figure 4.8 The zoom-in displays of the sinus structures of the head phantom. (a) without noise suppression; (b)with the proposed iterative noise suppression method. Display window: [0.1 0.8].

4.4 Conclusion and discussions

We derive a general framework of iterative de-noising for material decomposition of DECT. This method expands the application of the iterative noise suppression method from a linear decomposition model to a more complex, non-linear decomposition. With this expansion, the proposed method fully explores the benefits of dual energy imaging on beam-hardening artifacts correction. Using the proposed method, we reduce the decomposed image noise standard deviation by one order of magnitude on both Catphan©600 phantom and the head phantom, while still keeping a high spatial resolution. Compared to the conventional formulation of least square estimation with smoothness regularization, the proposed method improves the spatial resolution under the comparable background noise level. The non-linear decomposition model corrects for the beam-hardening artifacts, improves spatial uniformity, and obtains better image quality compared to the linear decomposition model.

The polynomial function used in this study is an empirical dual energy calibration method. It relies on a calibration phantom that must provide path length variations through the two basis material and combinations of path lengths through both materials.

Residual streaking artifacts can still be observed on the decomposed images. Future investigation on different calibration phantom designs is encouraged. The two CT images used in this study are reconstructed using standard FBP algorithm on the projections acquired with two scans of different spectra. To reduce the exposure to the patients, we will design the low-dose data acquisition schemes. For example, we can perform two scans, one with the normal x-ray exposure protocol while the other with a much lower tube current. Or we can keep the tube current the same for the two scans while reducing the number of projection views in each scan.

CHAPTER 5

SUMMARY AND FUTURE DIRECTIONS

In this dissertation, the limitations of x-ray kV CBCT imaging were investigated. A low-dose and scatter-free CBCT imaging method was studied in Chapter 2. This method uses a stationary beam blocker for scatter measurement, and an iterative reconstruction method to recover signals from incomplete primary signals. The beam blocker geometry was optimized using a simulation study, and the performance of the proposed method was evaluated using physical experiments. Chapter 3 and 4 investigated the noise boost problem in DECT. Iterative noise suppression algorithms using linear and non-linear decomposition models were proposed to improve image quality. The methods incorporate the decomposition function in the iterations of algorithm optimization such that spatial resolution is maintained with significantly reduced image noise. These algorithms were verified using phantom studies on the table-top system.

In Chapter 2, lead strips in the longitudinal direction are used as the beam blocker for scatter measurement. Other possible designs, like crossing-figure [81], or moving blockers [100], could achieves similar scatter correction performance. In the future, we will look into other possible beam blocker designs, and compare the resultant image quality. Dual energy imaging requires two projection measurements with different x-ray energies. To reduce the imaging dose, we can insert a half-field beam filter between the x-ray source and the object, such that any ray passing through the object is filtered once from one of the opposite directions in a single full scan. Projection measurements therefore are acquired with two different x-ray spectra without changing the tube energy. This method is based on the redundancy on the projection data. However, the central longitudinal line of the detector is measured only once, thus projection measurement with two different x-ray spectra is not possible in this region. Furthermore, the finite value of

focal spot size and beam filter thickness lead to penumbra effects, and measurement points that fall into the penumbra area cannot be used since the x-ray energy spectra is not consistent. Therefore, we cannot get sufficient dual energy data in a single scan. To alleviate this problem, we can compensate for the missing data with the data measured with another spectrum, for example, using polynomial fitting method.

APPENDIX

DEVIATION OF THE NOISE VARIANCE-COVARIANCE MATRIX OF DECOMPOSED IMAGES WITH A NON-LINEAR DECOMPOSITION MODEL

Since the noise of decomposed images at different pixels is independent, we have the variance-covariance matrix of the observation as,

$$W = \begin{pmatrix} \mathrm{cov}(d_{1,m}, d_{1,m}) \cdot I & \mathrm{cov}(d_{1,m}, d_{2,m}) \cdot I \\ \mathrm{cov}(d_{2,m}, d_{1,m}) \cdot I & \mathrm{cov}(d_{2,m}, d_{2,m}) \cdot I \end{pmatrix} \quad \text{Equation A1}$$

where $d_{1/2,m}$ is a pixel in basis material image. cov(.) calculates covariance.

If a linear reconstruction method is implemented, e.g. FBP, a pixel in the reconstructed image is a weighted summation of the line integrals,

$$d_{1/2,m} = \sum_{i}^{N_p} c_{i,m} \cdot l_{1/2,i} = \sum_{i}^{N_p} c_{i,m} \cdot f_{1/2}(p_{H,i}, p_{L,i}) \quad \text{Equation A2}$$

where $c_{i,m}$ is the coefficients of linear function which is determined by the system geometry and the reconstructed pixel position. N_p is pixel number of CT projections or basis material line integrals. Since the noise at different pixels of raw projections is also independent, the elements in the noise variance-covariance matrix are calculated as,

$$\mathrm{cov}(d_{1,m}, d_{1,m}) = \sum_{i}^{N_p} \left(c_{i,m}\right)^2 \cdot \mathrm{cov}\left(f_1(p_{H,i}, p_{L,i}), f_1(p_{H,i}, p_{L,i})\right) \quad \text{Equation A3}$$

$$\mathrm{cov}(d_{2,m}, d_{2,m}) = \sum_{i}^{N_p} \left(c_{i,m}\right)^2 \cdot \mathrm{cov}\left(f_2(p_{H,i}, p_{L,i}), f_2(p_{H,i}, p_{L,i})\right) \quad \text{Equation A4}$$

$$\mathrm{cov}(d_{1,m}, d_{2,m}) = \mathrm{cov}(d_{2,m}, d_{1,m}) = \sum_{i}^{N_p} \left(c_{i,m}\right)^2 \cdot \mathrm{cov}\left(f_1(p_{H,i}, p_{L,i}), f_2(p_{H,i}, p_{L,i})\right) \quad \text{Equation A5}$$

To obtain the noise variance-covariance matrix, we need to derive the covariance in the basis material line integrals.

$$\begin{aligned} \mathrm{cov}\left(f_1(p_{H,i}, p_{L,i}), f_2(p_{H,i}, p_{L,i})\right) &= E\left[\left(f_1(p_{H,i}, p_{L,i}) - \overline{f_1(p_{H,i}, p_{L,i})}\right)\left(f_2(p_{H,i}, p_{L,i}) - \overline{f_2(p_{H,i}, p_{L,i})}\right)\right] \\ &= E\left[f_1(p_{H,i}, p_{L,i}) f_2(p_{H,i}, p_{L,i})\right] - E\left[f_1(p_{H,i}, p_{L,i})\right] \cdot E\left[f_2(p_{H,i}, p_{L,i})\right] \end{aligned} \quad \text{Equation A6}$$

Using Taylor expansion and ignoring the high-order terms, we have

$$\begin{aligned} E\left[f_1(p_{H,i}, p_{L,i})\right] &\approx E\left[\begin{array}{l} f_1(\overline{p_{H,i}}, \overline{p_{L,i}}) + (p_{H,i} - \overline{p_{H,i}}) \dfrac{\partial f_1}{\partial p_H}(\overline{p_{H,i}}, \overline{p_{L,i}}) + (p_{L,i} - \overline{p_{L,i}}) \dfrac{\partial f_1}{\partial p_L}(\overline{p_{H,i}}, \overline{p_{L,i}}) \\ + \dfrac{1}{2!}(p_{H,i} - \overline{p_{H,i}})^2 \dfrac{\partial^2 f_1}{\partial {p_H}^2}(\overline{p_{H,i}}, \overline{p_{L,i}}) + \dfrac{1}{2!}(p_{L,i} - \overline{p_{L,i}})^2 \dfrac{\partial^2 f_1}{\partial {p_L}^2}(\overline{p_{H,i}}, \overline{p_{L,i}}) \\ + \dfrac{1}{2!}(p_{H,i} - \overline{p_{H,i}})(p_{L,i} - \overline{p_{L,i}}) \dfrac{\partial f_1}{\partial p_H} \dfrac{\partial f_1}{\partial p_L}(\overline{p_{H,i}}, \overline{p_{L,i}}) \end{array}\right] \\ &= f_1(\overline{p_{H,i}}, \overline{p_{L,i}}) + \frac{1}{2} \frac{\partial^2 f_1}{\partial {p_H}^2}(\overline{p_{H,i}}, \overline{p_{L,i}}) E\left[(p_{H,i} - \overline{p_{H,i}})^2\right] + \frac{1}{2} \frac{\partial^2 f_1}{\partial {p_L}^2}(\overline{p_{H,i}}, \overline{p_{L,i}}) E\left[(p_{L,i} - \overline{p_{L,i}})^2\right] \end{aligned} \quad \text{Equation A7}$$

Similarly,

$$E\left[f_2(p_{H,i},p_{L,i})\right]\approx f_2(\overline{p_{H,i}},\overline{p_{L,i}})+\frac{1}{2}\frac{\partial^2 f_2}{\partial p_H{}^2}(\overline{p_{H,i}},\overline{p_{L,i}})E\left[(p_{H,i}-\overline{p_{H,i}})^2\right]+\frac{1}{2}\frac{\partial^2 f_2}{\partial p_L{}^2}(\overline{p_{H,i}},\overline{p_{L,i}})E\left[(p_{L,i}-\overline{p_{L,i}})^2\right] \quad \text{Equation A8}$$

Denote $n_{pH/Li,}$ as the statistical noise of pixels in CT raw data, and the noise variance in the CT raw data is calculated as $\mathrm{var}(n_{pH,i})=E\left[(p_{H,i}-\overline{p_{H,i}})^2\right]$, $\mathrm{var}(n_{pL,i})=E\left[(p_{L,i}-\overline{p_{L,i}})^2\right]$, we can further simplify the above function as,

$$\begin{aligned}E\left[f_1(p_{H,i},p_{L,i})\right]\cdot E\left[f_2(p_{H,i},p_{L,i})\right]\approx{}& f_1(\overline{p_{H,i}},\overline{p_{L,i}})f_2(\overline{p_{H,i}},\overline{p_{L,i}})\\&+\frac{1}{2}f_2(\overline{p_{H,i}},\overline{p_{L,i}})\left[\frac{\partial^2 f_1}{\partial p_H{}^2}(\overline{p_{H,i}},\overline{p_{L,i}})\,\mathrm{var}(n_{pH,i})+\frac{\partial^2 f_1}{\partial p_L{}^2}(\overline{p_{H,i}},\overline{p_{L,i}})\,\mathrm{var}(n_{pL,i})\right]\\&+\frac{1}{2}f_1(\overline{p_{H,i}},\overline{p_{L,i}})\left[\frac{\partial^2 f_2}{\partial p_H{}^2}(\overline{p_{H,i}},\overline{p_{L,i}})\,\mathrm{var}(n_{pH,i})+\frac{\partial^2 f_2}{\partial p_L{}^2}(\overline{p_{H,i}},\overline{p_{L,i}})\,\mathrm{var}(n_{pL,i})\right]\end{aligned} \quad \text{Equation A9}$$

With Taylor expansion and ignoring the high order terms, we have

$$\begin{aligned}E\left[f_1(p_{H,i},p_{L,i})\cdot f_2(p_{H,i},p_{L,i})\right]\approx{}& f_1(\overline{p_{H,i}},\overline{p_{L,i}})f_2(\overline{p_{H,i}},\overline{p_{L,i}})\\&+\frac{\partial f_1}{\partial p_H}(\overline{p_{H,i}},\overline{p_L})\frac{\partial f_2}{\partial p_H}(\overline{p_{H,i}},\overline{p_{L,i}})\,\mathrm{var}(n_{pH,i})+\frac{\partial f_1}{\partial p_L}(\overline{p_{H,i}},\overline{p_{L,i}})\frac{\partial f_2}{\partial p_L}(\overline{p_{H,i}},\overline{p_{L,i}})\,\mathrm{var}(n_{pL,i})\\&+\frac{1}{2}f_1(\overline{p_{H,i}},\overline{p_{L,i}})\left[\frac{\partial^2 f_2}{\partial p_H{}^2}(\overline{p_{H,i}},\overline{p_L})\,\mathrm{var}(n_{pH,i})+\frac{\partial^2 f_2}{\partial p_L{}^2}(\overline{p_{H,i}},\overline{p_{L,i}})\,\mathrm{var}(n_{pL,i})\right]\\&+\frac{1}{2}f_2(\overline{p_{H,i}},\overline{p_{L,i}})\left[\frac{\partial^2 f_1}{\partial p_H{}^2}(\overline{p_{H,i}},\overline{p_{L,i}})\,\mathrm{var}(n_{pH,i})+\frac{\partial^2 f_1}{\partial p_L{}^2}(\overline{p_{H,i}},\overline{p_{L,i}})\,\mathrm{var}(n_{pL,i})\right]\end{aligned} \quad \text{Equation A10}$$

By substituting Equation A9 and Equation A10 into Equation A6, we have

$$\begin{aligned}\operatorname{cov}\left(f_1(p_{H,i},p_{L,i}),f_2(p_{H,i},p_{L,i})\right) &= E\left[f_1(p_{H,i},p_{L,i})\cdot f_2(p_{H,i},p_{L,i})\right]-E\left[f_1(p_{H,i},p_{L,i})\right]\cdot E\left[f_2(p_{H,i},p_{L,i})\right]\\ &\approx \frac{\partial f_1}{\partial p_{H,i}}(\overline{p_{H,i}},\overline{p_{L,i}})\frac{\partial f_2}{\partial p_H}(\overline{p_{H,i}},\overline{p_{L,i}})\operatorname{var}(n_{pH,i})+\frac{\partial f_1}{\partial p_L}(\overline{p_{H,i}},\overline{p_{L,i}})\frac{\partial f_2}{\partial p_L}(\overline{p_{H,i}},\overline{p_{L,i}})\operatorname{var}(n_{pL,i})\end{aligned}$$

Equation A11

Similarly, we have

$$\operatorname{cov}\left(f_1(p_{H,i},p_{L,i}),f_1(p_{H,i},p_{L,i})\right)\approx[\frac{\partial f_1}{\partial p_H}(\overline{p_{H,i}},\overline{p_{L,i}})]^2\operatorname{var}(n_{pH,i})+[\frac{\partial f_1}{\partial p_L}(\overline{p_{H,i}},\overline{p_{L,i}})]^2\operatorname{var}(n_{pL,i})$$

Equation A12

$$\operatorname{cov}\left(f_2(p_{H,i},p_{L,i}),f_2(p_{H,i},p_{L,i})\right)\approx[\frac{\partial f_2}{\partial p_H}(\overline{p_{H,i}},\overline{p_{L,i}})]^2\operatorname{var}(n_{pH,i})+[\frac{\partial f_2}{\partial p_L}(\overline{p_{H,i}},\overline{p_{L,i}})]^2\operatorname{var}(n_{pL,i})$$

Equation A13

By substituting Equation A11-A13 into Equation A3-A5, we have,

$$\operatorname{cov}(d_{1,m},d_{1,m})=\sum_i^{N_p}\left(c_{i,m}\right)^2\left\{[\frac{\partial f_1}{\partial p_H}(\overline{p_{H,i}},\overline{p_{L,i}})]^2\operatorname{var}(n_{pH,i})+[\frac{\partial f_1}{\partial p_L}(\overline{p_{H,i}},\overline{p_{L,i}})]^2\operatorname{var}(n_{pL,i})\right\}$$

Equation A14

$$\operatorname{cov}(d_{2,m},d_{2,m})=\sum_i^{N_p}\left(c_{i,m}\right)^2\left\{[\frac{\partial f_2}{\partial p_H}(\overline{p_{H,i}},\overline{p_{L,i}})]^2\operatorname{var}(n_{pH,i})+[\frac{\partial f_2}{\partial p_L}(\overline{p_{H,i}},\overline{p_{L,i}})]^2\operatorname{var}(n_{pL,i})\right\}$$

Equation A15

$$\operatorname{cov}(d_{1,m},d_{2,m})=\operatorname{cov}(d_{2,m},d_{1,m})=\sum_i^{N_p}\left(c_{i,m}\right)^2\left\{\frac{\partial f_1}{\partial p_{H,i}}(\overline{p_{H,i}},\overline{p_{L,i}})\frac{\partial f_2}{\partial p_H}(\overline{p_{H,i}},\overline{p_{L,i}})\operatorname{var}(n_{pH,i})+\frac{\partial f_1}{\partial p_L}(\overline{p_{H,i}},\overline{p_{L,i}})\frac{\partial f_2}{\partial p_L}(\overline{p_{H,i}},\overline{p_{L,i}})\operatorname{var}(n_{pL,i})\right\}$$

Equation A16

To simplify the calculation, we approximate $\frac{\partial f_{1/2}}{\partial p_{H/L}}(\overline{p_{H,i}}, \overline{p_{L,i}})$ at different pixels to its average value $\frac{\partial f_{1/2}}{\partial p_{H/L}}(p_H, p_L)$, and $\mathrm{var}(n_{pH/L,i})$ to the average value $\mathrm{var}(n_{pH/L})$. Since the noise variance on the projection data is difficult to obtain, we calculate the noise variance of a uniform area on the CT images to approximate the noise variance on the projection data. Equation A14-A16 can be simplified as,

$$\mathrm{cov}\left(f_1(p_{H,i}, p_{L,i}), f_1(p_{H,i}, p_{L,i})\right) \approx [\frac{\partial f_1}{\partial p_H}(p_H, p_L)]^2 \,\mathrm{var}(n_H) + [\frac{\partial f_1}{\partial p_L}(p_H, p_L)]^2 \,\mathrm{var}(n_L) \qquad \text{Equation A17}$$

$$\mathrm{cov}\left(f_2(p_{H,i}, p_{L,i}), f_2(p_{H,i}, p_{L,i})\right) \approx [\frac{\partial f_2}{\partial p_H}(p_H, p_L)]^2 \,\mathrm{var}(n_H) + [\frac{\partial f_2}{\partial p_L}(p_H, p_L)]^2 \,\mathrm{var}(n_L) \qquad \text{Equation A18}$$

$$\mathrm{cov}\left(f_1(p_{H,i}, p_{L,i}), f_2(p_{H,i}, p_{L,i})\right) \approx \frac{\partial f_1}{\partial p_H}(p_H, p_L) \cdot \frac{\partial f_2}{\partial p_H}(p_H, p_L) \cdot \mathrm{var}(n_H) + \frac{\partial f_1}{\partial p_L}(p_H, p_L) \cdot \frac{\partial f_2}{\partial p_L}(p_H, p_L) \cdot \mathrm{var}(n_L)$$

Equation A19

where $var(n_{H/L})$ calculates the noise variance on the CT images at high/low x-ray tube energies.

Equation A3, Equation A4 and Equation A5 are rewritten as,

$$\mathrm{cov}(d_{1,m}, d_{1,m}) \approx C \cdot \left\{ [\frac{\partial f_1}{\partial p_H}(p_H, p_L)]^2 \,\mathrm{var}(n_H) + [\frac{\partial f_1}{\partial p_L}(p_H, p_L)]^2 \,\mathrm{var}(n_L) \right\} \qquad \text{Equation A20}$$

$$\mathrm{cov}(d_{2,m}, d_{2,m}) \approx C \cdot \left\{ [\frac{\partial f_2}{\partial p_H}(p_H, p_L)]^2 \,\mathrm{var}(n_H) + [\frac{\partial f_2}{\partial p_L}(p_H, p_L)]^2 \,\mathrm{var}(n_L) \right\} \qquad \text{Equation A21}$$

$$\mathrm{cov}(d_{1,m}, d_{2,m}) = \mathrm{cov}(d_{2,m}, d_{1,m}) \approx C\left\{\frac{\partial f_1}{\partial p_H}(p_H, p_L)\cdot\frac{\partial f_2}{\partial p_H}(p_H, p_L)\cdot \mathrm{var}(n_H) + \frac{\partial f_1}{\partial p_L}(p_H, p_L)\cdot\frac{\partial f_2}{\partial p_L}(p_H, p_L)\cdot \mathrm{var}(n_L)\right\}$$

Equation A22

where $C = \sum_{i}^{N_p}\left(c_{i,m}\right)^2$

By substituting Equation A20, Equation A21 and Equation A22 into Equation A1, and approximating the value of *C* to be the same for different pixels, we have

$$W = C\cdot\begin{pmatrix} w_1\cdot I & w_3\cdot I \\ w_4\cdot I & w_2\cdot I \end{pmatrix}$$

Equation A23

The size of *W* is 2*N*x2*N*, and *N* is the pixel numbers in CT/decomposed images. And w_1, w_2, w_3, w_4 are calculated as,

$$w_1 = [\frac{\partial f_1}{\partial p_H}(p_H, p_L)]^2\ \mathrm{var}(n_H) + [\frac{\partial f_1}{\partial p_L}(p_H, p_L)]^2\ \mathrm{var}(n_L)$$

$$w_2 = [\frac{\partial f_2}{\partial p_H}(p_H, p_L)]^2\ \mathrm{var}(n_H) + [\frac{\partial f_2}{\partial p_L}(p_H, p_L)]^2\ \mathrm{var}(n_L)$$

$$w_3 = w_4 = \frac{\partial f_1}{\partial p_H}(p_H, p_L)\cdot\frac{\partial f_2}{\partial p_H}(p_H, p_L)\cdot \mathrm{var}(n_H) + \frac{\partial f_1}{\partial p_L}(p_H, p_L)\cdot\frac{\partial f_2}{\partial p_L}(p_H, p_L)\cdot \mathrm{var}(n_L)$$

The noise suppression algorithm incorporates a regularization to enforce image smoothness, and the balance between data fidelity and image regularization is controlled by the regularization weighting β. Therefore, we ignore the constant C in the noise variance-covariance function, and further simplify W as,

$$W = \begin{pmatrix} w_1 \cdot I & w_3 \cdot I \\ w_4 \cdot I & w_2 \cdot I \end{pmatrix} \qquad \text{Equation A24}$$

REFERENCES

[1] Jaffray, D.A. and J.H. Siewerdsen, *Cone-beam computed tomography with a flat-panel imager: initial performance characterization.* Med Phys, 2000. **27**(6): 1311-23.

[2] Swindell, W., R.G. Simpson, J.R. Oleson, C.T. Chen, and E.A. Grubbs, *Computed tomography with a linear accelerator with radiotherapy applications.* Med Phys, 1983. **10**(4): 416-20.

[3] Cho, P.S., R.H. Johnson, and T.W. Griffin, *Cone-beam CT for radiotherapy applications.* Phys Med Biol, 1995. **40**(11): 1863-83.

[4] Harrison, R.M. and F.T. Farmer, *Possible application of a radiotherapy simulator for imaging of body cross - sections.* Br J Radiol, 1976. **49**(585): 813.

[5] Niu, T.Y. and L. Zhu, *Overview of X-ray Scatter in Cone-beam Computed Tomography and Its Correction Methods.* Current Medical Imaging Reviews, 2010. **6**(2): 82-89.

[6] Guan, H. and H. Dong, *Dose calculation accuracy using cone-beam CT (CBCT) for pelvic adaptive radiotherapy.* Phys. Med. Biol., 2009. **54**(20): 6239-6250.

[7] Oldham, M., D. Létourneau, L. Watt, G. Hugo, D. Yan, D. Lockman, L.H. Kim, P.Y. Chen, A. Martinez, and J.W. Wong, *Cone-beam-CT guided radiation therapy: A model for on-line application.* Radiother. Oncol., 2005. **75**(3): 271-8.

[8] Niu, T., L. Zhu, and A. Al-Basheer, *Quantitative cone-beam CT imaging in radiation therapy using planning CT as a prior: First patient studies.* Med. Phy., 2012. **39**(4): 1991-2000.

[9] Fahrig, R., R. Dixon, T. Payne, R.L. Morin, A. Ganguly, and N. Strobel, *Dose and image quality for a cone-beam C-arm CT system.* Med. Phys., 2006. **33**(12): 4541-4550.

[10] Lauritsch, G., J. Boese, L. Wigström, H. Kemeth, and R. Fahrig, *Towards Cardiac C-Arm Computed Tomography.* IEEE Trans. Med. Imag., 2006. **25**(7): 922-934.

[11] Scarfe, W.C., A.G. Farman, and P. Sukovic, *Clinical applications of cone-beam computed tomography in dental practice.* J Can Dent Assoc, 2006. **72**(1): 75-80.

[12] De Vos, W., J. Casselman, and G.R. Swennen, *Cone-beam computerized tomography (CBCT) imaging of the oral and maxillofacial region: a systematic review of the literature.* Int J Oral Maxillofac Surg, 2009. **38**(6): 609-25.

[13] Zhu, L., J. Wang, and L. Xing, *Noise suppression in scatter correction for cone-beam CT.* Med Phys, 2009. **36**(3): 741-52.

[14] Johns, P.C. and M. Yaffe, *Scattered radiation in fan beam imaging systems.* Med Phys, 1982. **9**(2): 231-9.

[15] Joseph, P.M. and R.D. Spital, *The effects of scatter in x-ray computed tomography.* Med Phys, 1982. **9**(4): 464-72.

[16] Glover, G.H., *Compton scatter effects in CT reconstructions.* Med Phys, 1982. **9**(6): 860-7.

[17] Endo, M., S. Mori, T. Tsunoo, and H. Miyazaki, *Magnitude and effects of x-ray scatter in a 256-slice CT scanner.* Med Phys, 2006. **33**(9): 3359-68.

[18] Siewerdsen, J.H. and D.A. Jaffray, *Cone-beam computed tomography with a flat-panel imager: magnitude and effects of x-ray scatter.* Med Phys, 2001. **28**(2): 220-31.

[19] Wang, G., H. Yu, and B. De Man, *An outlook on x-ray CT research and development.* Med Phys, 2008. **35**(3): 1051-64.

[20] Engel, K.J., C. Herrmann, and G. Zeitler, *X-ray scattering in single- and dual-source CT.* Med Phys, 2008. **35**(1): 318-32.

[21] Siewerdsen, J.H., M.J. Daly, B. Bakhtiar, D.J. Moseley, S. Richard, H. Keller, and D.A. Jaffray, *A simple, direct method for x-ray scatter estimation and correction in digital radiography and cone-beam CT.* Med Phys, 2006. **33**(1): 187-97.

[22] Ning, R., X. Tang, and D. Conover, *X-ray scatter correction algorithm for cone beam CT imaging.* Medical physics, 2004. **31**(5): 1195-202.

[23] Wagner, F.C., A. Macovski, and D.G. Nishimura, *Dual-energy x-ray projection imaging: two sampling schemes for the correction of scattered radiation.* Med Phys, 1988. **15**(5): 732-48.

[24] Yaffe, M.J. and P.C. Johns, *Scattered Radiation in Diagnostic-Radiology - Magnitudes, Effects, and Methods of Reduction.* Journal of Applied Photographic Engineering, 1983. **9**(6): 184-195.

[25] Seibert, J.A. and J.M. Boone, *X-Ray Scatter Removal by Deconvolution.* Medical Physics, 1988. **15**(4): 567-575.

[26] Zellerhoff, M., B. Scholz, E.P. Ruhrnschopf, and T. Brunner, *Low contrast 3D-reconstruction from C-arm data.* Medical Imaging 2005: Physics of Medical Imaging, Pts 1 and 2, 2005. **5745**: 646-655.

[27] Li, H., R. Mohan, and X.R. Zhu, *Scatter kernel estimation with an edge-spread function method for cone-beam computed tomography imaging.* Physics in Medicine and Biology, 2008. **53**(23): 6729-6748.

[28] Hansen, V.N., W. Swindell, and P.M. Evans, *Extraction of primary signal from EPIDs using only forward convolution.* Medical physics, 1997. **24**(9): 1477-84.

[29] Kyriakou, Y., T. Riedel, and W.A. Kalender, *Combining deterministic and Monte Carlo calculations for fast estimation of scatter intensities in CT.* Physics in Medicine and Biology, 2006. **51**(18): 4567-4586.

[30] Kwan, A.L., J.M. Boone, and N. Shah, *Evaluation of x-ray scatter properties in a dedicated cone-beam breast CT scanner.* Med Phys, 2005. **32**(9): 2967-75.

[31] Shen, S.Z., A.K. Bloomquist, G.E. Mawdsley, M.J. Yaffe, and I. Elbakri, *Effect of scatter and an antiscatter grid on the performance of a slot-scanning digital mammography system.* Med Phys, 2006. **33**(4): 1108-15.

[32] Siewerdsen, J.H., D.J. Moseley, B. Bakhtiar, S. Richard, and D.A. Jaffray, *The influence of antiscatter grids on soft-tissue detectability in cone-beam computed tomography with flat-panel detectors.* Med Phys, 2004. **31**(12): 3506-20.

[33] Schmidt, T.G., R. Fahrig, N.J. Pelc, and E.G. Solomon, *An inverse-geometry volumetric CT system with a large-area scanned source: a feasibility study.* Med Phys, 2004. **31**(9): 2623-7.

[34] Krol, A., D.A. Bassano, C.C. Chamberlain, and S.C. Prasad, *Scatter reduction in mammography with air gap.* Med Phys, 1996. **23**(7): 1263-70.

[35] Maalej, N., M.A. Al Kafi, A. Nobah, and A.A. Naqvi, *Air Gap Effect on Mammography Image Quality.* World Congress on Medical Physics and Biomedical Engineering 2006, Vol 14, Pts 1-6, 2007. **14**: 1401-1404.

[36] Neitzel, U., *Grids or air gaps for scatter reduction in digital radiography: a model calculation.* Med Phys, 1992. **19**(2): 475-81.

[37] Brenner, D.J. and E.J. Hall, *Computed tomography--an increasing source of radiation exposure.* N Engl J Med, 2007. **357**(22): 2277-84.

[38] Sykes, J.R., A. Amer, J. Czajka, and C.J. Moore, *A feasibility study for image guided radiotherapy using low dose, high speed, cone beam X-ray volumetric imaging.* Radiotherapy and oncology : journal of the European Society for Therapeutic Radiology and Oncology, 2005. **77**(1): 45-52.

[39] Sorensen, S.P., P.E. Chow, S. Kriminski, P.M. Medin, and T.D. Solberg, *Image-guided radiotherapy using a mobile kilovoltage x-ray device.* Medical dosimetry : official journal of the American Association of Medical Dosimetrists, 2006. **31**(1): 40-50.

[40] Murphy, M.J., J. Balter, S. Balter, J.A. BenComo, Jr., I.J. Das, S.B. Jiang, C.M. Ma, G.H. Olivera, R.F. Rodebaugh, K.J. Ruchala, H. Shirato, and F.-F. Yin, *The management of imaging dose during image-guided radiotherapy: report of the AAPM Task Group 75.* Medical physics, 2007. **34**(10): 4041-63.

[41] Kan, M.W., L.H. Leung, W. Wong, and N. Lam, *Radiation dose from cone beam computed tomography for image-guided radiation therapy.* Int J Radiat Oncol Biol Phys, 2008. **70**(1): 272-9.

[42] Ding, G.X. and C.W. Coffey, *Radiation dose from kilovoltage cone beam computed tomography in an image-guided radiotherapy procedure.* Int J Radiat Oncol Biol Phys, 2009. **73**(2): 610-7.

[43] Paul, J., B. Schell, J.M. Kerl, W. Maentele, T.J. Vogl, and R.W. Bauer, *Effect of contrast material on image noise and radiation dose in adult chest computed tomography using automatic exposure control: a comparative study between 16-, 64- and 128-slice CT.* Eur J Radiol, 2011. **79**(2): e128-32.

[44] Matsumoto, K., Y. Ohno, H. Koyama, A. Kono, H. Inokawa, Y. Onishi, M. Nogami, D. Takenaka, T. Araki, and K. Sugimura, *3D automatic exposure control for 64-detector row CT: radiation dose reduction in chest phantom study.* Eur J Radiol, 2011. **77**(3): 522-7.

[45] Gomi, S., Y. Muramatsu, S. Tsukagoshi, M. Suzuki, R. Kakinuma, R. Tsuchiya, and N. Moriyama, *Low-dose CT screening for lung cancer with automatic exposure control: phantom study.* Radiol Phys Technol, 2008. **1**(2): 244-50.

[46] Mulkens, T.H., P. Bellinck, M. Baeyaert, D. Ghysen, X. Van Dijck, E. Mussen, C. Venstermans, and J.-L. Termote, *Use of an automatic exposure control mechanism for dose optimization in multi-detector row CT examinations: clinical evaluation.* Radiology, 2005. **237**(1): 213-23.

[47] Svalkvist, A. and M. Bath, *The benefit of accounting for DQE variations in simulated dose reduction of digital radiographic systems.* Radiat Prot Dosimetry, 2010. **139**(1-3): 57-61.

[48] Wang, Y., L.E. Antonuk, Q.H. Zhao, Y. El-Mohri, and L. Perna, *High-DQE EPIDs based on thick, segmented BGO and CsI:Tl scintillators: Performance evaluation at extremely low dose.* Medical Physics, 2009. **36**(12): 5707-5718.

[49] Wang, J., T. Li, H.B. Lu, and Z.R. Liang, *Penalized weighted least-squares approach to sinogram noise reduction and image reconstruction for low-dose X-ray computed tomography.* Ieee Transactions on Medical Imaging, 2006. **25**(10): 1272-1283.

[50] Kalender, W.A., E. Klotz, and L. Kostaridou, *An algorithm for noise suppression in dual energy CT material density images.* IEEE Trans Med Imaging, 1988. **7**(3): 218-24.

[51] Balvay, D., N. Kachenoura, S. Espinoza, I. Thomassin-Naggara, L.S. Fournier, O. Clement, and C.A. Cuenod, *Signal-to-noise ratio improvement in dynamic contrast-enhanced CT and MR imaging with automated principal component analysis filtering.* Radiology, 2011. **258**(2): 435-45.

[52] Zhang, X., R. Ning, and D. Yang, *Cone Beam Breast CT noise reduction using 3D adaptive Gaussian filtering.* Journal of X-Ray Science and Technology, 2009. **17**(4): 319-33.

[53] Sidky, E.Y. and X. Pan, *Image reconstruction in circular cone-beam computed tomography by constrained, total-variation minimization.* Phys Med Biol, 2008. **53**(17): 4777-807.

[54] Jia, X., Y. Lou, R. Li, W.Y. Song, and S.B. Jiang, *GPU-based fast cone beam CT reconstruction from undersampled and noisy projection data via total variation.* Med Phys, 2010. **37**(4): 1757-60.

[55] Zeng, G.L., R. Clack, and G.T. Gullberg, *Implementation of Tuy's cone-beam inversion formula.* Physics in medicine and biology, 1994. **39**(3): 493-507.

[56] Hsieh, J., R.C. Molthen, C.A. Dawson, and R.H. Johnson, *An iterative approach to the beam hardening correction in cone beam CT.* Med Phys, 2000. **27**(1): 23-9.

[57] Draenert, F.G., E. Coppenrath, P. Herzog, S. Muller, and U.G. Mueller-Lisse, *Beam hardening artefacts occur in dental implant scans with the NewTom cone beam CT but not with the dental 4-row multidetector CT.* Dento maxillo facial radiology, 2007. **36**(4): 198-203.

[58] Kachelriess, M., K. Sourbelle, and W.A. Kalender, *Empirical cupping correction: a first-order raw data precorrection for cone-beam computed tomography.* Med Phys, 2006. **33**(5): 1269-74.

[59] Alvarez, R.E. and A. Macovski, *Energy-selective reconstructions in X-ray computerized tomography.* Phys Med Biol, 1976. **21**(5): 733-44.

[60] Sidky, E.Y., Y. Zou, and X.C. Pan, *Impact of polychromatic x-ray sources on helical, cone-beam computed tomography and dual-energy methods.* Physics in Medicine and Biology, 2004. **49**(11): 2293-2303.

[61] Stenner, P., T. Berkus, and M. Kachelriess, *Empirical dual energy calibration (EDEC) for cone-beam computed tomography.* Med Phys, 2007. **34**(9): 3630-41.

[62] Graser, A., T.R. Johnson, M. Bader, M. Staehler, N. Haseke, K. Nikolaou, M.F. Reiser, C.G. Stief, and C.R. Becker, *Dual energy CT characterization of urinary calculi: initial in vitro and clinical experience.* Invest Radiol, 2008. **43**(2): 112-9.

[63] Ogle, G.D., J.R. Allen, I.R. Humphries, P.W. Lu, J.N. Briody, K. Morley, R. Howman-Giles, and C.T. Cowell, *Body-composition assessment by dual-energy x-ray absorptiometry in subjects aged 4-26 y.* Am J Clin Nutr, 1995. **61**(4): 746-53.

[64] Johnson, T.R., B. Krauss, M. Sedlmair, M. Grasruck, H. Bruder, D. Morhard, C. Fink, S. Weckbach, M. Lenhard, B. Schmidt, T. Flohr, M.F. Reiser, and C.R. Becker, *Material differentiation by dual energy CT: initial experience.* Eur Radiol, 2007. **17**(6): 1510-7.

[65] Deng, K., C. Liu, R. Ma, C. Sun, X.M. Wang, Z.T. Ma, and X.L. Sun, *Clinical evaluation of dual-energy bone removal in CT angiography of the head and neck: comparison with conventional bone-subtraction CT angiography.* Clinical Radiology, 2009. **64**(5): 534-541.

[66] Thieme, S.F., C.R. Becker, M. Hacker, K. Nikolaou, M.F. Reiser, and T.R.C. Johnson, *Dual energy CT for the assessment of lung perfusion-Correlation to scintigraphy.* European Journal of Radiology, 2008. **68**(3): 369-374.

[67] Yeh, B.M., J.A. Shepherd, Z.J. Wang, H.S. Teh, R.P. Hartman, and S. Prevrhal, *Dual-energy and low-kVp CT in the abdomen.* AJR Am J Roentgenol, 2009. **193**(1): 47-54.

[68] Kelcz, F., P.M. Joseph, and S.K. Hilal, *Noise considerations in dual energy CT scanning.* Med Phys, 1979. **6**(5).

[69] Chandarana, H., M.C. Godoy, I. Vlahos, A. Graser, J. Babb, C. Leidecker, and M. Macari, *Abdominal aorta: evaluation with dual-source dual-energy multidetector*

CT after endovascular repair of aneurysms--initial observations. Radiology, 2008. **249**(2): 692-700.

[70] Fletcher, J.G., N. Takahashi, R. Hartman, L. Guimaraes, J.E. Huprich, D.M. Hough, L. Yu, and C.H. McCollough, *Dual-energy and dual-source CT: is there a role in the abdomen and pelvis?* Radiologic clinics of North America, 2009. **47**(1): 41-57.

[71] Matsumoto, K., M. Jinzaki, Y. Tanami, A. Ueno, M. Yamada, and S. Kuribayashi, *Virtual monochromatic spectral imaging with fast kilovoltage switching: improved image quality as compared with that obtained with conventional 120-kVp CT.* Radiology, 2011. **259**(1): 257-62.

[72] Tanguay, J., H.K. Kim, and I.A. Cunningham, *The role of x-ray Swank factor in energy-resolving photon-counting imaging.* Med Phys, 2010. **37**(12): 6205-11.

[73] Zhang, K., G. Rosenbaum, and G. Bunker, *Energy-resolving X-ray fluorescence detection using synthetic multilayers.* Journal of synchrotron radiation, 1998. **5**(Pt 4): 1227-34.

[74] Zou, Y., X. Pan, and E.Y. Sidky, *Image reconstruction in regions-of-interest from truncated projections in a reduced fan-beam scan.* Phys Med Biol, 2005. **50**(1): 13-27.

[75] Niu, T. and L. Zhu, *Accelerated barrier optimization compressed sensing (ABOCS) reconstruction for cone-beam CT: phantom studies.* Med Phys, 2012. **39**(7): 4588-98.

[76] Tsaig, Y. and D.L. Donoho, *Extensions of compressed sensing.* Signal Processing, 2006. **86**(3): 549-571.

[77] Sidky, E.Y., C.M. Kao, and X.H. Pan, *Accurate image reconstruction from few-views and limited-angle data in divergent-beam CT.* Journal of X-Ray Science and Technology, 2006. **14**(2): 119-139.

[78] Tian, Z., X. Jia, K. Yuan, T. Pan, and S.B. Jiang, *Low-dose CT reconstruction via edge-preserving total variation regularization.* Phys Med Biol, 2011. **56**(18): 5949-67.

[79] Zhu, L., Y. Xie, J. Wang, and L. Xing, *Scatter correction for cone-beam CT in radiation therapy.* Med Phys, 2009. **36**(6): 2258-68.

[80] Dong, X., X. Jia, T.Y. Niu, and L. Zhu, *Low-dose and Scatter-free Cone-beam CT imaging: a preliminary study.* Medical Imaging 2012: Physics of Medical Imaging, 2012. **8313**.

[81] Niu, T. and L. Zhu, *Scatter correction for full-fan volumetric CT using a stationary beam blocker in a single full scan.* Med Phys, 2011. **38**(11): 6027-38.

[82] Endo, M., T. Tsunoo, N. Nakamori, and K. Yoshida, *Effect of scattered radiation on image noise in cone beam CT.* Med Phys, 2001. **28**(4): 469-74.

[83] Siewerdsen, J.H. and D.A. Jaffray, *Optimization of x-ray imaging geometry (with specific application to flat-panel cone-beam computed tomography).* Med Phys, 2000. **27**(8): 1903-14.

[84] Boone, J.M. and J.A. Seibert, *An analytical model of the scattered radiation distribution in diagnostic radiology.* Med Phys, 1988. **15**(5): 721-5.

[85] Gao, H., R. Fahrig, N.R. Bennett, M. Sun, J. Star-Lack, and L. Zhu, *Scatter correction method for x-ray CT using primary modulation: phantom studies.* Med Phys, 2010. **37**(2): 934-46.

[86] Gao, H., L. Zhu, and R. Fahrig, *Modulator design for x-ray scatter correction using primary modulation: material selection.* Med Phys, 2010. **37**(8): 4029-37.

[87] Zhu, L., N.R. Bennett, and R. Fahrig, *Scatter correction method for X-ray CT using primary modulation: Theory and preliminary results.* Ieee Transactions on Medical Imaging, 2006. **25**(12): 1573-1587.

[88] Maltz, J.S., W.-E. Blanz, D. Hristov, and A. Bani-Hashemi, *Cone beam X-ray scatter removal via image frequency modulation and filtering.* Conf Proc IEEE Eng Med Biol Soc, 2005. **2**: 1854-7.

[89] Colijn, A.P. and F.J. Beekman, *Accelerated simulation of cone beam X-ray scatter projections.* IEEE Trans Med Imaging, 2004. **23**(5): 584-90.

[90] Kyriakou, Y., T. Riedel, and W.A. Kalender, *Combining deterministic and Monte Carlo calculations for fast estimation of scatter intensities in CT.* Physics in medicine and biology, 2006. **51**(18): 4567-86.

[91] Maltz, J.S., B. Gangadharan, M. Vidal, A. Paidi, S. Bose, B.A. Faddegon, M. Aubin, O. Morin, J. Pouliot, Z. Zheng, M.M. Svatos, and A.R. Bani-Hashemi, *Focused beam-stop array for the measurement of scatter in megavoltage portal and cone beam CT imaging.* Med Phys, 2008. **35**(6): 2452-62.

[92] Wagner, F.C., A. Macovski, and D.G. Nishimura, *Dual-energy x-ray projection imaging: two sampling schemes for the correction of scattered radiation.* Medical physics, 1988. **15**(5): 732-48.

[93] Kyriakou, Y., M. Meyer, and W.A. Kalender, *Technical note: comparing coherent and incoherent scatter effects for cone-beam CT.* Phys Med Biol, 2008. **53**(10): N175-85.

[94] Niu, T., M. Sun, J. Star-Lack, H. Gao, Q. Fan, and L. Zhu, *Shading correction for on-board cone-beam CT in radiation therapy using planning MDCT images.* Medical physics, 2010. **37**(10): 5395-406.

[95] Feldkamp, L.A., L.C. Davis, and J.W. Kress, *Practical Cone-Beam Algorithm.* Journal of the Optical Society of America a-Optics Image Science and Vision, 1984. **1**(6): 612-619.

[96] Zhu, L., N. Strobel, and R. Fahrig, *X-ray scatter correction for cone-beam CT using moving blocker array.* Medical Imaging 2005: Physics of Medical Imaging, Pts 1 and 2, 2005. **5745**: 251-258.

[97] Cho, S., T. Lee, J. Min, and H. Chung, *Feasibility study on many-view under-sampling technique for low-dose computed tomography.* Optical Engineering, 2012. **51**(8).

[98] Pua, R., J. Min, B. Yoo, K.-W. Kim, G. Cho, and S. Cho. *Backprojection-filtration image reconstruction from partial cone-beam data for scatter correction*. in *Proc. SPIE 7961, Medical Imaging 2011: Physics of Medical Imaging*. 2011.

[99] Dong, X., T. Niu, X. Jia, and L. Zhu, *Relationship between x-ray illumination field size and flat field intensity and its impacts on x-ray imaging.* Med Phys, 2012. **39**(10): 5901-9.

[100] Wang, J., W. Mao, and T. Solberg, *Scatter correction for cone-beam computed tomography using moving blocker strips: a preliminary study.* Med Phys, 2010. **37**(11): 5792-800.

[101] Carrier, J.-F., L. Archambault, L. Beaulieu, and R. Roy, *Validation of GEANT4, an object-oriented Monte Carlo toolkit, for simulations in medical physics.* Med Phys, 2004. **31**(3).

[102] Jia, X., H. Yan, L. Cervino, M. Folkerts, and S.B. Jiang, *A GPU tool for efficient, accurate, and realistic simulation of cone beam CT projections.* Med Phys, 2012. **39**(12): 7368-78.

[103] Zhu, L., S. Yoon, and R. Fahrig, *A short-scan reconstruction for cone-beam CT Using shift-invariant FBP and equal weighting.* Medical Physics, 2007. **34**(11): 4422-4438.

[104] Zhu, L., J. Starman, and R. Fahrig, *An efficient estimation method for reducing the axial intensity drop in circular cone-beam CT.* Int J Biomed Imaging, 2008. **2008**: 242841.

[105] Brockmann, C., S. Jochum, M. Sadick, K. Huck, P. Ziegler, C. Fink, S.O. Schoenberg, and S.J. Diehl, *Dual-energy CT angiography in peripheral arterial occlusive disease.* Cardiovasc Intervent Radiol, 2009. **32**(4): 630-7.

[106] Tran, D.N., M. Straka, J.E. Roos, S. Napel, and D. Fleischmann, *Dual-energy CT discrimination of iodine and calcium: experimental results and implications for lower extremity CT angiography.* Acad Radiol, 2009. **16**(2): 160-71.

[107] Watanabe, Y., K. Uotani, T. Nakazawa, M. Higashi, N. Yamada, Y. Hori, S. Kanzaki, T. Fukuda, T. Itoh, and H. Naito, *Dual-energy direct bone removal CT angiography for evaluation of intracranial aneurysm or stenosis: comparison with conventional digital subtraction angiography.* Eur Radiol, 2009. **19**(4): 1019-24.

[108] Thieme, S.F., V. Graute, K. Nikolaou, D. Maxien, M.F. Reiser, M. Hacker, and T.R. Johnson, *Dual Energy CT lung perfusion imaging--correlation with SPECT/CT.* Eur J Radiol, 2012. **81**(2): 360-5.

[109] Zhang, L.J., C.S. Zhou, U.J. Schoepf, H.X. Sheng, S.Y. Wu, A.W. Krazinski, J.R. Silverman, F.G. Meinel, Y.E. Zhao, Z.J. Zhang, and G.M. Lu, *Dual-energy CT lung ventilation/perfusion imaging for diagnosing pulmonary embolism.* Eur Radiol, 2013.

[110] Ruzsics, B., H. Lee, P.L. Zwerner, M. Gebregziabher, P. Costello, and U.J. Schoepf, *Dual-energy CT of the heart for diagnosing coronary artery stenosis and myocardial ischemia-initial experience.* Eur Radiol, 2008. **18**(11): 2414-24.

[111] De Cecco, C.N., V. Buffa, S. Fedeli, M. Luzietti, A. Vallone, R. Ruopoli, V. Miele, M. Rengo, P. Paolantonio, M. Maurizi Enrici, A. Laghi, and V. David, *Dual energy CT (DECT) of the liver: conventional versus virtual unenhanced images.* Eur Radiol, 2010. **20**(12): 2870-5.

[112] Graser, A., T.R. Johnson, H. Chandarana, and M. Macari, *Dual energy CT: preliminary observations and potential clinical applications in the abdomen.* Eur Radiol, 2009. **19**(1): 13-23.

[113] Primak, A.N., J.G. Fletcher, T.J. Vrtiska, O.P. Dzyubak, J.C. Lieske, M.E. Jackson, J.C. Williams, Jr., and C.H. McCollough, *Noninvasive differentiation of uric acid versus non-uric acid kidney stones using dual-energy CT.* Acad Radiol, 2007. **14**(12): 1441-7.

[114] Warp, R.J. and J.T. Dobbins, *Quantitative evaluation of noise reduction strategies in dual-energy imaging.* Med Phys, 2003. **30**(2): 190-8.

[115] Macovski, A., D.G. Nishimura, A. Doost-Hoseini, and W.R. Brody, *Measurement-Dependent Filtering: A Novel Approach to Improved SNR.* IEEE Trans Med Imaging, 1983. **2**(3): 122-7.

[116] Zou, Y. and M.D. Silver, *Analysis of fast kV-switching in dual energy CT using a pre-reconstruction decomposition technique - art. no. 691313.* Medical Imaging 2008: Physics of Medical Imaging, Pts 1-3, 2008. **6913**: 91313-91313.

[117] Szczykutowicz, T.P. and G.H. Chen, *Dual energy CT using slow kVp switching acquisition and prior image constrained compressed sensing.* Phys Med Biol, 2010. **55**(21): 6411-29.

[118] Maass, C., M. Baer, and M. Kachelriess, *Image-based dual energy CT using optimized precorrection functions: A practical new approach of material decomposition in image domain.* Medical Physics, 2009. **36**(8): 3818-3829.

[119] Rutherford, R., B. Pullan, and I. Isherwoord, *Measurement of effective atomic number and electron density using an EMI scanner.* Neuroradiology 1976. **11**: 15-21.

[120] Rutherford, R.A., B.R. Pullan, and I. Isherwood, *X-Ray Energies for Effective Atomic Number Determination.* Neuroradiology, 1976. **11**(1): 23-28.

[121] Nishimura, D.G., A. Macovski, and W.R. Brody, *Noise reduction methods for hybrid subtraction.* Med Phys, 1984. **11**(3): 259-65.

[122] Fessler, J.A., I. Elbakri, P. Sukovic, and N.H. Clinthorne, *Maximum-likelihood dual-energy tomographic image reconstruction.* Medical Imaging 2002: Image Processing, Vol 1-3, 2002. **4684**: 38-49.

[123] Zhang, R., J.-B. Thibault, Member, C.A. Bouman, K.D. Sauer, and J. Hsieh. *A Model-Based Iterative Algorithm forDual-Energy X-Ray CT Reconstruction*. in *proceedings of the Second International Conference on Image Formation in X-Ray Computed Tomography*. 2012. Salt Lake City, Utah.

[124] Sidky, E.Y. and X.C. Pan, *Accurate image reconstruction in circular cone-beam computed tomography by total variation minimization: a preliminary investigation.* 2006 Ieee Nuclear Science Symposium Conference Record, Vol 1-6, 2006: 2904-2907.

[125] Siddon, R.L., *Fast Calculation of the Exact Radiological Path for a 3-Dimensional Ct Array.* Medical Physics, 1985. **12**(2): 252-255.

[126] Chandarana, H., A.J. Megibow, B.A. Cohen, R. Srinivasan, D. Kim, C. Leidecker, and M. Macari, *Iodine quantification with dual-energy CT: phantom study and preliminary experience with renal masses.* AJR Am J Roentgenol, 2011. **196**(6): W693-700.

[127] Flohr, T.G., C.H. McCollough, H. Bruder, M. Petersilka, K. Gruber, C. Suss, M. Grasruck, K. Stierstorfer, B. Krauss, R. Raupach, A.N. Primak, A. Kuttner, S. Achenbach, C. Becker, A. Kopp, and B.M. Ohnesorge, *First performance evaluation of a dual-source CT (DSCT) system.* Eur Radiol, 2006. **16**(2): 256-68.

[128] Thibault, J.B., K.D. Sauer, C.A. Bouman, and J. Hsieh, *A three-dimensional statistical approach to improved image quality for multislice helical CT.* Med Phys, 2007. **34**(11): 4526-44.

[129] Bouman, C. and K. Sauer, *A generalized Gaussian image model for edge-preserving MAP estimation.* IEEE Trans Image Process, 1993. **2**(3): 296-310.

[130] Sukovic, P. and N.H. Clinthorne, *Penalized weighted least-squares image reconstruction for dual energy X-ray transmission tomography.* IEEE Trans Med Imaging, 2000. **19**(11): 1075-81.

[131] Niu, T., X. Dong, M. Petrongolo, and L. Zhu, *Iterative image-domain decomposition for dual-energy CT.* Med Phys, 2014. **14**(4): 041901.

[132] Alvarez, R.E., *Dimensionality and noise in energy selective x-ray imaging.* Med Phys, 2013. **40**(11): 111909.

[133] Dong, X., T.Y. Niu, and L. Zhu, *Single-scan energy-selective imaging on cone-beam CT: a preliminary study.* Medical Imaging 2013: Physics of Medical Imaging, 2013. **8668**.

[134] Zhang, G.W., J.P. Cheng, L. Zhang, Z.Q. Chen, and Y.X. Xing, *A practical reconstruction method for dual energy computed tomography.* Journal of X-Ray Science and Technology, 2008. **16**(2): 67-88.

[135] Hinshaw, D.A. and J.T. Dobbins, *Recent progress in noise reduction and scatter correction in dual-energy imaging.* Medical Imaging 1995 - Physics of Medical Imaging, 1995. **2432**: 134-142.

[136] Strutz, T., *Data Fitting and Uncertainty: A Practical Introduction to Weighted Least Squares and Beyond*. 2010: Vieweg and Teubner.

[137] Niu, T., A. Al-Basheer, and L. Zhu, *Quantitative cone-beam CT imaging in radiation therapy using planning CT as a prior: first patient studies.* Medical physics, 2012. **39**(4): 1991-2000.